JOURNAL OF MATERIALS RESEARCH AND TECHNOLOGY 2022;18:2993–3025

Available online at www.sciencedirect.com

jmr&t Journal of Materials Research and Technology

journal homepage: www.elsevier.com/locate/jmrt

Review Article

Review on modeling and simulation of dynamic recrystallization of martensitic stainless steels during bulk hot deformation

Hamed Aghajani Derazkola[*], *Eduardo Garcia*, *Alberto Murillo-Marrodán*, *Aintzane Conde Fernandez*

Department of Mechanics, Design and Industrial Management, University of Deusto, 48007 Bilbao, Spain

ARTICLE INFO

Article history:
Received 18 February 2022
Accepted 28 March 2022
Available online 4 April 2022

Keywords:
Martensitic stainless steel
Hot deformation
Dynamic recrystallization
Mathematical modeling

ABSTRACT

Bulk hot deformation is a relatively old manufacturing technique widely adopted in different industry fields to form and shape different metallic alloys. Martensitic stainless steels (MSS) are a class of metals used in industries with extreme conditions. Hot forming of this class of steels is a highly complex process comprising several highly coupled thermo-chemo-physical phenomena. The complex microstructural changes of MSS make it challenging to develop an overall system of governing equations for theoretically analyzing the behavior of MSS during the hot deformation process. Modeling and simulation analysis have frequently been used to minimize the number of experiments often used to find MSS behavior during hot deformations. This review paper deals with the latest developments in the numerical analysis of material behavior, microstructural simulation, and artificial intelligence methods for MSS during the hot deformation process. Important numerical issues in macro and micro-scale models, such as various materials flow modeling, finite element methods, cellular automaton, and artificial neural networks, are discussed. Macro-scale analysis of hot deformation will allow many manufacturing processes to understand the effects of changes in different strain and strain rates before physical testing. Micro-scale analysis of hot deformation will allow understanding physical phenomena concerning dynamic recrystallization, plastic deformation energy, and microstructure size. The main methods used in the MSS hot deformation process simulation are discussed and illustrated with brief case studies. In addition, several critical vital problems and issues remain to be addressed about this topic, and opportunities for further research are identified.

* Corresponding author.
E-mail address: h.aghajani@deusto.es (H. Aghajani Derazkola).

https://doi.org/10.1016/j.jmrt.2022.03.179

1. Introduction

Martensitic Stainless Steels (MSS) were developed mainly to improve stainless steels' hardness, strength, and wear resistance [1]. This purpose is achieved because they can be hardened by heat treatment thanks to the transformation of austenite into martensite by air quenching and tempering [2]. MSS are usually ternary alloys of iron with Chromium (Cr) content between 10.5 and 18 weight percent (Wt.%), and a Carbon (C) content generally around 0.02 Wt.% or less, although in some cases it can exceed 1.2% [3]. Despite not being one of its main characteristics, the presence of carbides helps to increase wear resistance for some specific applications [4]. This way, the grades with higher carbon content are alloyed with other elements such as niobium, silicon, tungsten, and vanadium, to form carbides that increase MSS wear resistance [5].

In some cases, small amounts of nickel are added to MSS to improve corrosion resistance and toughness [6]. Martensitic stainless steels have high thermal conductivity, making them suitable for applications that require good heat distribution, such as heat exchangers [7]. Furthermore, their low Coefficient of Thermal Expansion (CTE) makes them more likely to retain their shape at high temperatures [8]. They are also used in aerospace applications, where a high degree of stiffness is required, thanks to their high Young's modulus [9]. The general applications of MSS include cutlery, steam and gas turbine blades, bushings, etc [10]. In MSS, with increased contains chromium and carbon, the hardness and corrosion resistance are improved [11]. Its applications include measuring instruments, ball bearings, gauge blocks, molds, and dies, etc [12]. There are also sub-grades 440A, 440B, and 440C with varying amounts of carbon to increase/reduce its hardness and toughness [13].

Classification of stainless steels can be done from an application point of view, where three types are usually found: low to medium carbon (0.10–0.30 Wt. %), with a minimum Cr content to be stainless steels (12 Wt.%), high carbon content (0.60–1.20 Wt.%) with an increased Cr content to overcome the carbon excess, Cr (16–18 Wt.%) [14–19]. This composition is characterized by higher mechanical and corrosion resistance [20]. Finally, a group of cold-work die steels is characterized by high corrosion and wear resistance [1]. The metallurgical classification of MSS can also be drawn with three types of steel [21]. The first category is usually hardened by precipitation of iron or alloy carbides when tempered [22]. With a lower carbon content, the second type of these steels increases its hardness thanks to the precipitation of copper or intermetallic particles during tempering [23]. Finally, the third class corresponds to precipitation-strengthened MSS, steels with low carbon content, although additional alloy elements favor the precipitation of second-phase particles for hardening like NiAl, NiTi, Ni_3Ti, and Ni_3Be [4].

The wide range of stainless-steel applications, which demand is increasing, requires improvements in the most commonly used manufacturing methods [24]. Among them, hot forming is one of the most extended production processes, where a proper knowledge of the material behavior in the hot condition is of great importance [25]. During hot forming, the strain hardening effect is compensated by dynamic recovery (DRV) and dynamic recrystallization (DRX) [26]. These three phenomena control the material flow stress during its deformation at different temperatures and strain rates. During the deformation of metals, defects (mainly dislocations) are created in their crystal structure [27]. Increasing dislocations also increases the deformation resistance of the material, causing strain hardening [28]. However, individual dislocations or pairs of dislocations are annihilated, forming subgrains that act as sinks for moving dislocations, reducing, thus, the resistance of the material [29–31]. This phenomenon is known as dynamic recovery, DRV, which has an essential effect on high stacking-fault-energy (SFE) metals (e.g., aluminum and its alloys, iron in ferrite phase, and titanium alloys the beta phase, or MSS). The dynamic recovery leads to low stresses at high temperatures favoring high ductility [32].

Dynamic recrystallization is the nucleation and growth of new grains during the hot deformation of metals [33]. It typically occurs at high strains and above half of melting temperature (T_m) and is favored by high temperatures and low strain rates [34,35]. There are three types of DRX which are discontinuous dynamic recrystallization (dDRX), continuous dynamic recrystallization (cDRX), and geometric dynamic recrystallization (gDRX) [36]. In cDRX, dislocations are progressively absorbed into the grains' boundaries, which leads to increasing misorientations, which finally give rise to an equiaxed structure of high angle boundaries [37]. This recrystallization mechanism is typical of high stacking-fault-energy metals, such as MSS [38]. In low-SFE materials (e.g., iron and steel, not the case of MSS) at high temperatures, DRV is not important since grain boundaries achieve high mobility leading to relevant differences in dislocation density across the grain boundaries [39]. Hence, new strain-free grains arise via the discontinuous dynamic recrystallization process, dDRX. Finally, gDRX occurs at high strain conditions due to grain elongation and thinning, causing the grains to collapse each other leading to fragmentation [40].

In this paper a comprehensive review of the most important approaches developed for modelling and simulation of recrystallization of martensitic stainless steels during bulk hot forming deformation is presented. For that purpose, the manuscript has been divided into 5 main sections. After this introduction which is Section 1, the main parameters obtained from experimentation and used in the mathematical modelization of hot bulk metal forming are gathered in Section 2. Next, in Section 3 the constitutive models for material flow in MSS are summarized. Then, in Section 4 the approaches for modelling the microstructure evolution during dynamic recrystallization of MSS are gathered. Finally, the Artificial Neural Networks application in flow stress prediction of MSS are reviewed.

2. Mathematical parameters in dynamic recrystallization of MSS

2.1. *Bulk hot deformation characteristic point*

Experimental tests usually accomplish the study of metal's behavior in hot conditions [41]. The most commonly used for the characterization of the behavior of metals at high temperature is

the hot compression test, where a specimen is compressed under a specific combination of temperature and strain rate, which are kept constant during the test [42]. The temperature and strain rate conditions are varied in order to cover the wide range of studies. Additional information regarding this test can be found in the standard ASTM E209 – 18 [43].

A typical result of the data obtained from the test is shown in Fig. 1, where the evolution of true stress is plotted as a function of the true strain. From this graph, some critical aspects can be identified. For instance, at the very beginning of the curve, the true stress increases sharply due to WH. Subsequently, dynamic recovery causes a reduction in the hardening rate [44]. Afterwards, the dynamic recrystallization starts, which also reduces the hardening rate. The point at which the DRX starts is the critical point that is determined by the critical stress (σ_c) and the critical strain (ε_c) [45]. DRX and DRV counterbalance the WH reaching a peak in the curve, from where the stress no longer increases. The peak stress determines this peak point (σ_p) and the peak strain (ε_p) [46]. The stress usually decreases from that point due to DRX reaching a plateau in the curve starting on the steady-state strain (ε_s), at a stress value of (σ_s) [47]

These points, commonly known as the characteristic points, are usually extracted from the experimental curves for each temperature and strain rate combination. Their values vary depending on the test conditions [48]. Fortunately, this variation is not random, and it is possible to establish relations between deformation conditions and the characteristic points [49].

The dependence of peak and steady-state stress, σ_p, and σ_s, on deformation conditions, can be computed from experimental data with different approaches in the case of Martensitic Stainless Steels [50].

As in most steel, in MSS, the increase of temperature or the decrease of strain rate shifts all characteristics points to lower stresses and strains. This implies that higher temperatures and lower strain rates favor the occurrence of DRX. Accordingly, most researchers have established relations between the characteristic points σ_p, σ_s and ε_p, ε_s, and the Zener-Hollomon parameter (Z). In some cases, potential relations between Z and the characteristic points were used, as those showed in Eqs. (1)–(4).

$$\sigma_s = A \cdot Z^b \tag{1}$$

$$\sigma_p = C \cdot Z^d \tag{2}$$

$$\varepsilon_p = E \cdot Z^f \tag{3}$$

$$\varepsilon_s = G \cdot Z^h \tag{4}$$

whose parameters are obtained from experimental data by adjusting the variation of $ln\sigma_p$ or $ln\sigma_s$ with lnZ, and the variation of $ln\ \varepsilon_p$ *or* $ln\ \varepsilon_s$ with lnZ [51,52].

Alternatively, logarithmic expressions have also been used for relating characteristic points with *the* Z parameter. Kevanlo et al. [53] obtained an excellent correlation using expressions such as that of Eq. (5), and Momeni et al. [54,55] considered the dimensionless parameter Z/A for this proposal, as it can be seen in Eqs. (6) and (7), being A the material constant in the hyperbolic sine function proposed by Sellars and Tegart [56]. The values of the constants for these equations were inferred by comparing the evolution of the characteristic points, and the logarithm of Z. The obtained equations are gathered in Table:

$$\sigma_s = A \cdot \ln Z - B \tag{5}$$

$$\sigma_p = a + bl_n\left(\frac{Z}{A}\right) \tag{6}$$

$$\sigma_s = c + dl_n\left(\frac{Z}{A}\right) \tag{7}$$

Interestingly, Momeni and Dehghani [55] point out that the expressions shown in Table 1 for AISI 410 are not accurate at low and high flow stress levels. Therefore, they propose specific equations for the low and high-stress levels. Specifically,

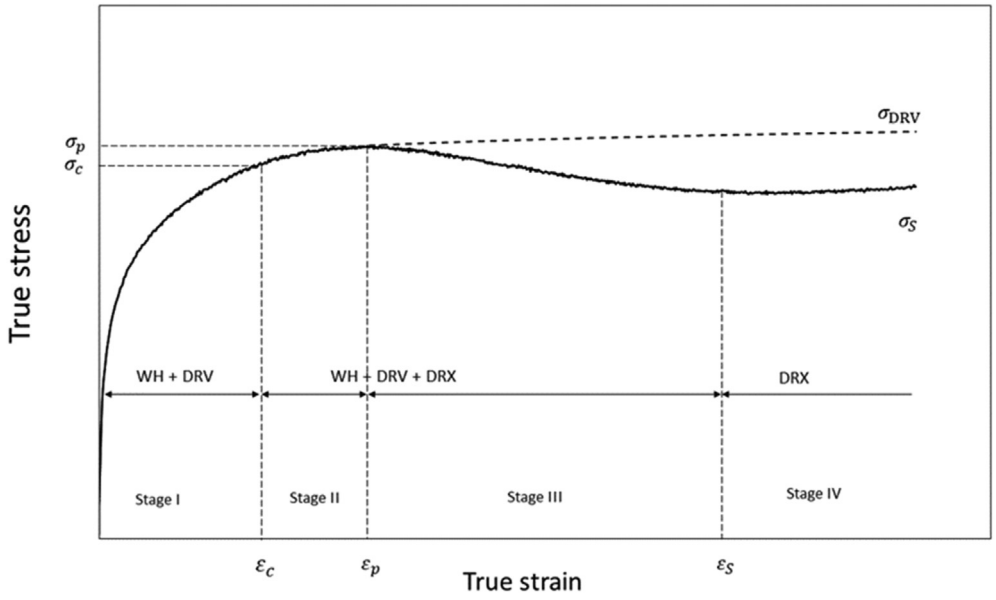

Fig. 1 – Point characterization of MSS.

they presented a nonlinear relationship between Z and σ_p being, Eq. (8) the one proposed for low flow stress, and Eq. (9) for high flow stress:

$$Z = 1.71 \cdot 10^6 \sigma_p^5 \tag{8}$$

$$Z = 1.78 \cdot 10^{14} \exp(0.06\sigma_P) \tag{9}$$

which is completed with the dependency of the peak strain and steady-state strain with Z parameter:

$$\varepsilon_P = 8.3 \cdot 10^{-3} Z^{0.11} \tag{10}$$

$$\varepsilon_s = 1.8 \cdot 10^{-2} \cdot Z^{0.072} \tag{11}$$

The obtention of these relationships is a necessary step for the development and determination of the material behaviour laws, and in consequence the modelling of the dynamic recrystallization.

2.2. *Critical points of dynamic recrystallization*

Of especial interest are the critical points of strain and stress, which are the points where dynamic recrystallization starts for the different deformation conditions.

According to the approach of Poliak and Jonas [60] the critical points can be obtained by analyzing the evolution of the strain hardening rate ($\theta = d\sigma/d\varepsilon$) as a function of the flow stress. The plot of these variables allows determining σ_p as the point at which the strain hardening rate equals zero ($\theta = 0$), and the inflection point of this curve indicates the critical stress (σ_c).

Table 1 – Experimental relationships between Z and the characteristic points.

Material	Relationships	Reference
AISI 410	$\varepsilon_p = 0.003 \cdot Z^{0.12}$	[52,57]
	$\sigma_p = 0.27 \cdot Z^{0.15}$	
	$\varepsilon_c = 0.0007 \cdot Z^{0.09}$	
	$\varepsilon_s = 0.015 \cdot Z^{0.093}$	
	$\sigma_s = 0.33 \cdot Z^{0.14}$	
X20Cr13	$\varepsilon_p = 0.0128 \cdot Z^{0.1082}$	[58]
	$\sigma_p = 1.02947 \cdot Z^{0.1509}$	
	$\varepsilon_s = 0.0058 \cdot Z^{0.1615}$	
	$\sigma_s = 2.1179 \cdot Z^{0.1468}$	
13%Cr MSS	$\varepsilon_p = 0.0006 \cdot Z^{0.43}$	[59]
	$\sigma_p = 0.145 \cdot Z^{0.37}$	
	$\varepsilon_c = 0.00028 \cdot Z^{0.45}$	
	$\sigma_c = 0.27 \cdot Z^{0.33}$	
AISI 410	$\sigma_p = 13.14 \cdot \ln\left(\frac{Z}{A}\right) - 92.93$	[51,55]
	$\sigma_s = 8.36 \cdot \ln\left(\frac{Z}{A}\right) + 75.29$	
	$\ln \varepsilon_p = 0.072 \cdot \ln Z - 3.99$	
	$\ln \varepsilon_s = 0.11 \cdot \ln Z - 4.79$	
AISI 403	$\sigma_p = 9.032 \cdot \ln(Z) - 267.54$	[53]
	$\varepsilon_p = 0.0259 \cdot \ln(Z) - 0.59$	
	$\sigma_c = 7.94 \cdot \ln(Z) - 236.86$	
	$\varepsilon_c = 0.0125 \cdot \ln(Z) - 0.28$	
	$\sigma_s = 7.022 \cdot \ln(Z) - 200.14$	
	$\varepsilon_s = 0.0456 \cdot \ln(Z) - 1.12$	

In addition, the evolution of strain hardening rate as a function of the true strain helps determining two interesting values of strain: the strain at which the rate of dynamic softening is maximized, ε^*, which corresponds with the minimum of these plots; and the steady-state strain, ε_s, which can be localized when the strain hardening reaches zero and the flow stress follows the almost constant trend. It also allows identifying the deformation conditions where fully recrystallization occurs because are those conditions whose θ evolution follows the explained trend, and the deformation conditions where dynamic recrystallization is partial because θ does not reach zero after the minimum.

Kassner and Barrabes [40] performed this study for a 13%Cr martensitic stainless steel obtaining the peak stress and the critical stress as an exponential function of Z [9], which have been gathered in Table 1.

Following the modification proposed by Najafizadeh and Jonas [61], Ahmadabadi et al. [44] drawn a third order equation for the experimental evolution of θ vs σ, starting from the yield point up to the σ_p for a 422 MSS.

$$\theta = A\sigma^3 + B\sigma^2 + C\sigma + D \tag{12}$$

Equating the second derivative to zero, the inflection point can be obtained:

$$\frac{d^2\theta}{d\sigma^2} = 0 \rightarrow 6A + 2B = 0 \rightarrow \sigma_C = -\frac{B}{3A} \tag{13}$$

A, B, C, and D, are material constants for a given set of hot deformation parameters. His experimental results obtained the critical stress to peak stress ratio of 0.84 for the 422 MSS [44].

Based also on the works of Jonas Poliak and Najafizadeh, the approach of proposes obtaining the critical points by using as a starting point a new equation that relates flow stress and strain presented by Eq. (14):

$$\frac{\sigma}{\sigma_p} = 1 - \exp\left(\Psi\left(\frac{\varepsilon}{\varepsilon_P}\right)^{\zeta}\right) \tag{14}$$

Being ψ, ζ, material constants whose values for the material studied, X20Cr13, are 3.6029 and 0.4787, respectively. The strain hardening rate is obtained from the derivative of Eq. (14), and the second derivative equalized to zero leads to the critical strain presented by Eq. (15):

$$\frac{\varepsilon_c}{\varepsilon_P} = \left(\frac{1}{\Psi\zeta}\right)^{1/\zeta} \tag{15}$$

This finally gives, as a result, the following relationship between critical strain, peak strain, and work hardening for X20Cr13:

$$\varepsilon_c = 0.32\varepsilon_P = 0.004096 \cdot z^{0.1082} \tag{16}$$

These are the research works using the Zenner-Hollomon parameter. As mentioned previously, there is another approach. Mizardeh and Najafzadeh [62] pointed out that the Zener-Hollomon parameter was not valid in the case of the hot behavior of the 17–4 PH precipitation hardening martensitic stainless steel. Since the effect of strain rate and temperature is opposite in Z, the experimental results from hot compression tests concluded that both strain rate and temperature favor recrystallization. To obtain this conclusion,

Mizardeh and Najafzadeh [62] analyzed the effect of the strain rate on the rate of DRX separately and the effect of temperature on the rate of DRX, obtaining the following expressions:

$$R_{DR|X} = \frac{1}{t_{0.3}} \propto \dot{\varepsilon} \tag{17}$$

$$R_{DR|X} = \frac{1}{t_{0.5}} \propto T^{5.59} \tag{18}$$

Finally, for considering the combined effect of both strain rate and temperature, the dynamic recrystallization rate parameter (DRXRP) was considered,

$$DRXRP = (\dot{\varepsilon})^a T^b \tag{19}$$

whose parameters were adjusted by relating $t_{0.5}$ and DRXRP, leading to the following expression:

$$R_{DRX} = \frac{1}{t_{0.5}} = 2.25 \cdot 10^{-15} - DRXRP^{0.87} \tag{20}$$

3. Constitutive models for material flow in MSS

The constitutive models are used to explain the relation existing between the flow stress of metals and alloys and their loading conditions. These relations are built based on experimental observations to describe the hot deformation behavior of the material in a form that can be used in computer codes. A distinction can be made between micro-mechanical constitutive relations and micro-mechanical constitutive models. The first ones use mathematical expressions to describe the material response and microstructure changes at a macroscopic scale by only using experimental testing such as hot compression testing. On the contrary, micro-mechanical constitutive models are based on crystal plasticity and crystallographic dislocation-density-based hardening and require microstructure observations.

This section provides the most relevant constitutive models in bulk metal forming, which have been developed to describe the evolution of flow stress and dynamic recrystallization as a function of material loading conditions.

3.1. *Arrhenius type equations*

The Arrhenius type is one of the most widespread constitutive equations that establish the relationship between hot deformation parameters, including flow stress, deformation temperature, and strain rate. Based on the hyperbolic sine function proposed by Sellars and Tegart [63] demonstrated that hot working could be considered a thermally-activated process expressed by strain rate equations similar to those used in creep. In this mathematical model, the Zener–Hollomon parameter Z expresses the combined effect of strain rate and temperature on material flow stress at a certain material strain [64]. Accordingly, the following set of equations is obtained [56]:

$$Z = \dot{\varepsilon} \exp\left(\frac{Q}{RT}\right) = f(\sigma) \tag{21}$$

$$\dot{\varepsilon} = \begin{cases} A_1 \sigma^{n_1} \exp\left(\dfrac{-Q}{RT}\right), & \alpha\sigma < 0.8 \\ A_2 \exp(\beta\sigma) \exp\left(\dfrac{-Q}{RT}\right), & \alpha\sigma > 1.2 \\ A_3 [\sin h(\alpha\sigma)]^n \exp\left(\dfrac{-Q}{RT}\right), & \text{for all } \sigma \end{cases} \tag{22-24}$$

where $\dot{\varepsilon}$ is strain rate (s^{-1}), T is the temperature (K), Q is the activation energy for dynamic recrystallization (kJ/mol), R is the universal gas constant (8.314 J/mol K), σ is the flow stress at a specific strain (MPa) and A, n, n_1, α, and β are material constants which are independent on temperature and strain rate [65]. Regarding the stress multiplier α, it can be described by $\alpha = \beta/n_1$. McQueen and Ryan [66] stated that its value increases as long as the number of solute elements in the alloy increases. They reported that stainless steels, such as MSS, show higher values (α = 0.017–0.025 MPa^{-1}) than low alloy steel (α = 0.012–0.014 MPa^{-1}).

As a result, three different relations can be defined for the constitutive material modeling. On the one hand, the power-law relationship is precise at low-stress values (Eq. 22) and, on the contrary, the exponential law described by Eq. 23 is suitable under high-stress values (high strain rates and/or low temperatures). Finally, the hyperbolic sine law presented in Eq. 24, is valid for the entire range of stress values [56].

Based on the flow stress curves of the material, in Fig. 2, a flow chart with the step-by-step procedure that has to be followed for the definition of the material constants is provided. The first step is the simplification and redefinition of the relations of Eq. 22 and Eq. 23. They can be reformulated, resulting in:

$$\dot{\varepsilon} = A_2 \sigma^{n_1} \exp\left(\frac{-Q}{RT}\right) = B \cdot \sigma^{n_1} \tag{25}$$

$$\dot{\varepsilon} = A_3 \exp(\beta\sigma) \exp\left(\frac{-Q}{RT}\right) = C \exp(\beta\sigma) \tag{26}$$

where B and C are temperature-dependent material constants. Then, if the logarithm of both sides of Eqs. (25) and (26) is taken, the following equations are obtained, respectively:

$$\ln(\sigma) = \frac{1}{n_1} \ln(\dot{\varepsilon}) - \frac{1}{n_1} \ln(B) \tag{27}$$

$$\sigma = \frac{1}{\beta} ln(\dot{\varepsilon}) - \frac{1}{\beta} \ln(C) \tag{28}$$

In addition, the logarithmic form of the hyperbolic sine law described in Eq. 24 can adopt the following formula:

$$\ln[\sin h(\alpha\sigma)] = \ln\left(\frac{\dot{\varepsilon}}{n}\right) + \left(\frac{Q}{nRT}\right) - \ln\left(\frac{A}{n}\right) \tag{29}$$

Then, the material constants β and n_1 can be obtained from the experimental values of flow stress and their corresponding strain rate at a particular strain. These constants correspond to the average values resulting from the slope of the curves in the plots of σ-ln $\dot{\varepsilon}$ and ln σ-ln $\dot{\varepsilon}$, respectively. In these plots, the slopes show approximately a similar value for all the considered deformation temperatures. Afterward, the value of the stress multiplier α is obtained from the expression $\alpha = \beta/n_1$, and the inverse slope of ln[sinh(α σ)] - ln $\dot{\varepsilon}$ is used for

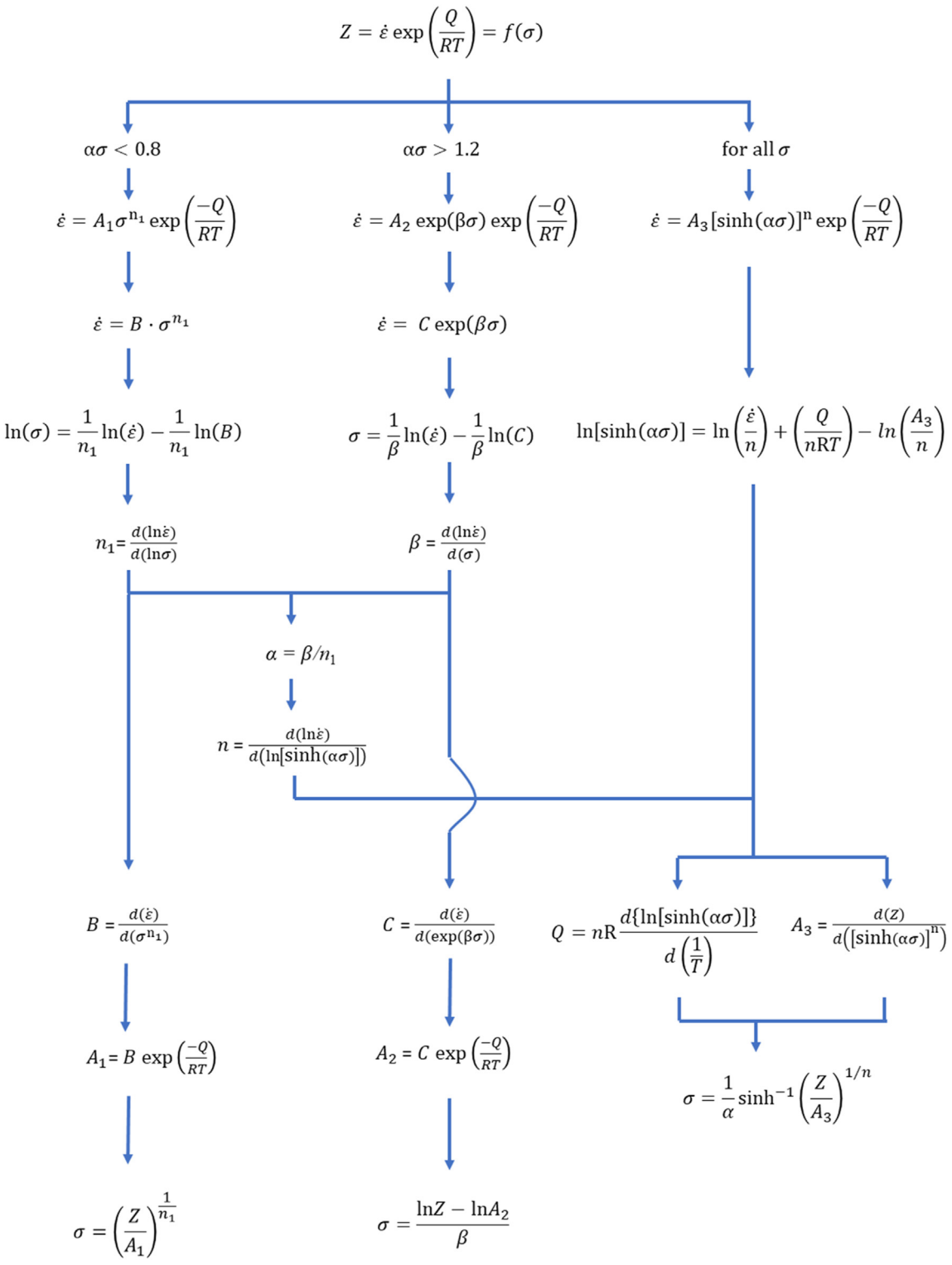

Fig. 2 – The calculation flow chart of constant parameters related to Arrhenius type constitutive equations.

calculating the value of n. Then, by differentiating Eq. 29, the value of the activation energy Q at a specific strain rate can be obtained from the mean slopes of ln[sinh($\alpha\ \sigma$)] - 1/ T plots, which results in

$$Q = n\cdot R\cdot\frac{d\{\ln[\sin h(\alpha\sigma)]\}}{d\left(\frac{1}{T}\right)} \quad (30)$$

Moreover, A value in Eq. 29 at a particular strain can be estimated by plotting ln Z - [sinh($\alpha\ \sigma$)] at a given strain. Finally, the material constants B and C can be calculated from the average values resulting from the curves' slope in the plots of Z-σ^{n_1} and Z-exp ($\beta\sigma$), respectively. In the whole material constant determination procedure, characteristic stresses such as peak, steady, or stress corresponding to a specific

Table 2 – Martensitic stainless steels activation energy, stress multiplier, and working condition.

MSS grade	Activation energy Q (kJ/mol)	Stress multiplier (MPa^{-1})	Working condition	Reference
AISI 422	420	0.0092	$\varepsilon = 0.1$	[44]
Super 13 Cr	432	0.01	Saturation stress	[70]
12Cr–10Ni	547.17	0.00064	$\varepsilon = 0.2$	[71]
AISI 420	399	0.008287	$\varepsilon = 0.1$	[72]
AISI 414	403	0.014	$\varepsilon = 0.4$	[73]
30Cr15Mo1N	503.5	0.00617	Peak stress	[74]
FV520B	911.97	0.0062	$\varepsilon = 0.15$	[75]
14Cr–4Ni	439	0.0082	$\varepsilon = 0.5$	[76]
Nitrogen-bearing MSS	453	0.009147	$\varepsilon = 0.2$	[77]
17-4 PH	337	0.011	Peak stress	[78]
AISI 410	448	0.011	Peak stress	[51]
AISI 410	205	0.00924	Peak stress	[79]
X20Cr13	359.4	0.00757	$\varepsilon = 0.5$	[80]
AISI 420	363.31	0.0082	Peak stress	[80]
AISI 410	374.93	0.0092	$\varepsilon = 0.3$	[81]
1Cr12Ni3Mo2VNbN	487.05	0.008	$\varepsilon = 0.2$	[82]
403Nb MSS	367.29	0.0153	Peak stress	[83]
1Cr12Ni2Mo2WVNb	470.43	0.0066	Peak stress	[84]
12CrNiMoWV	540.42	0.0077	$\varepsilon = 0.4$	[85]
05Cr17Ni4Cu4Nb	426.82	0.0106	Peak stress	[86]
00Cr13Ni5Mo2	439	0.0067	$\varepsilon = 0.1$ to 0.9	[87]

strain can be used [67,68]. Finally, all the defined material constants can be substituted into Eq. 24, yielding a valid constitutive equation at a certain strain and for all the considered stress range. According to the definition of the hyperbolic law, the flow stress can also be written as:

$$\sigma = \frac{1}{\alpha} \ln \left\{ \left(\frac{Z}{A}\right)^{1/n} + \left[\left(\frac{Z}{A}\right)^{2/n} + 1 \right]^{1/2} \right\} \tag{31}$$

The process for determining the material constants involved in the aforementioned formulation requires an experimental procedure to study the hot deformation behavior of the material. In the case of MSS, the general procedure consists of using uniaxial isothermal compression tests performed under the objective ranges of strain rate and temperature. Nevertheless, Oliveira et al. [69] analyzed the softening mechanisms of the AISI 410 MSS using isothermal torsion tests showing satisfactory results. In Table 2, the values of activation energy and the stress multiplier of reviewed MSS are gathered.

These results show that the stress multiplier shows low values compared to the stainless-steel values reported by McQueen and Ryan [66]. Moreover, the activation energy results are coherent with the reported values of similar materials in the literature. However, as can be appreciated in the case of AISI 410 and 420 steels, the election of a specific strain value or the peak stress of the material influences the characterization of the material constants. The Arrhenius type constitutive equation described by Eqs. (21)–(27) is only valid for the specific deformation condition in which the value of the material constant has been studied. In the Equation, the flow stress is independent of the deformation of the material, and thus, it can be considered a limiting factor. Hence, to extend the domain in which the constitutive model is valid, different strategies have been carried out.

On the one hand, Kishor et al. extended the domain of the proposed constitutive Equation for a 13Cr–4Ni MSS by analyzing the material constants α and n for true strains ranging from 0.1 to 0.69. These values were used in the final form of the hyperbolic sine equation; even so, the activation energy and A values were taken as constant. Nevertheless, at this point, the constitutive relation is still not dependent on the strain. The other approach is called strain compensation, which makes the material constants dependent on the strain. This dependency is established by using polynomial equations that fit the material parameter's value at different strains. In the literature, polynomials from third to ninth order have been effectively used in the material parameters fitting [84,85]. Xiao et al. [82] proposed a different approach for the 1Cr12Ni3Mo2VNbN martensitic steel to define the flow stress dependence on the strain. From the observation of the experimental stress–strain curves, the following relation was introduced:

$$\sigma = \beta_0 \varepsilon^{\beta_1} \cdot \exp(-\beta_2 \varepsilon) \tag{32}$$

where β_0 to β_2 are material constants. This relation was introduced in the hyperbolic sine equation yielding:

$$\sigma = \frac{\beta_0}{\alpha} \varepsilon^{\beta_1} \cdot \exp(-\beta_2 \varepsilon) \ln \left\{ \left(\frac{Z}{A}\right)^{1/n} + \left[\left(\frac{Z}{A}\right)^{2/n} + 1 \right]^{1/2} \right\} \tag{33}$$

The Arrhenius equations determined the material constants A, α, n, β, and Q. The material constants β_0 to β_2 were obtained using nonlinear regression, based on the least-squares method. As their value is not constant but dependent on deformation conditions such as strain rate and temperature, a linear regression technique was used to find a relation with the Zener-Hollomon parameter, yielding:

$$\beta_0 = 0.0049 \cdot \ln Z + 0.228 \tag{34}$$

$$\beta_1 = 0.014 \cdot \ln Z - 0.256 \tag{35}$$

$$\beta_2 = -0.009 \cdot \ln Z + 1.569 \tag{36}$$

The modified Arrhenius model showed a better agreement with the experimental flow stresses at lower temperatures than those at higher temperatures. Han et al. [75] used the strain compensation in developing the constitutive Equation to predict the FV520B flow stress. However, the model consistently underestimated the flow stress value at all strain rates under different temperature conditions. Therefore, they improved the constitutive model by the compensation of strain rate. The general strain rate compensation procedure consists of modifying the exponent of strain rate in Z [88,89]. However, for this material, it did not provide any improvement, and a different approach was proposed according to the following set of equations:

$$\ln Z^{*} = \ln(\varnothing\dot{\varepsilon}) + \frac{Q}{RT} \tag{37}$$

$$\varepsilon_{exp} = \varnothing\dot{\varepsilon} \tag{38}$$

$$\varnothing = A + B\dot{\varepsilon} \tag{39}$$

$$\varnothing = 2.66252 - 0.1343\dot{\varepsilon} \tag{40}$$

where $\varnothing$ is the function of strain rate, and it is obtained from the linear regression model. The constants A and B are determined from the known values of strain rate. The experimental flow stress and material constants are introduced into the hyperbolic sine equation to define the value at the particular strain rate. At a particular strain rate, many different values of $\dot{\varepsilon}_{exp}$ are obtained because the calculation of $\dot{\varepsilon}_{exp}$ is held at different experimental temperatures. However, the effect of the temperature on the value of $\dot{\varepsilon}_{exp}$ is sufficiently small that it could be neglected. Hence, the average values of $\dot{\varepsilon}_{exp}$ at a particular strain rate are used as the final value for the calculation $\varnothing$. Finally, the least square method is used to define the value of constants A and B. The strain rate compensated constitutive equation resulted in:

$$\sigma = \frac{1}{\alpha}\ln\left\{\left(\frac{Z^{*}}{A}\right)^{1/n} + \left[\left(\frac{Z^{*}}{A}\right)^{2/n} + 1\right]^{1/2}\right\} \tag{41}$$

As a result, the modified Equation could predict the stress more precisely than the one only considering the compensation of strain presented in Eq. (27).

Arrhenius type equations are recurrently used to analyze material parameters such as the activation energy, as well as to reproduce the flow stress of the material using hyperbolic sine relations combined with strain or strain rate compensation. However, their use to model the material flow in bulk hot deformation is not as extended as their use in the investigation of the material physical parameters.

3.2. *Avrami - JMAK*

A helpful approach for modeling dynamic recrystallization during hot working of steels is a modified version of the Avrami formulation, known as the Johnson-Mehl-Avrami-Kokmogorv (JMAK) equation:

$$X = 1 - \exp(-k \cdot t^{n}) \tag{42}$$

where X denotes the fractional softening, t represents time, and k and n are material constants. The DRX process causes a decrease in flow stress after the work-hardening stage leading to a peak in the flow curve of the hot compression test. Several research works use this Equation for considering this effect in the constitutive material model of MSS.

Considering that the progress of DRX is strain-dependent, this Equation has been adapted from time dependant to strain dependant. Accordingly, the deformation time from the beginning of recrystallization can be written [90]:

$$t = \frac{\varepsilon - \varepsilon_{c}}{\varepsilon^{*}} \tag{43}$$

where ε is the strain, ε_{c} represents the critical strain or the strain at which DRX starts (0.6–0.8 of peak strain, ε_{p}), and ε^{*} is the strain for maximum recrystallization. The determination of ε^{*} in Eq. (34) has led to different approaches in the case of MSS. The $\dot{\varepsilon}$, as shown in Eq. (22) leading to the JMAK equation:

$$t = \frac{\varepsilon - \varepsilon_{c}}{\dot{\varepsilon}} \tag{44}$$

$$X = 1 - \exp\left(-0.693\left(\frac{\varepsilon - \varepsilon_{c}}{\dot{\varepsilon}}\right)^{n}\right) \tag{45}$$

Another approach was the use of the strain required for 50 percent of recrystallization, $\varepsilon_{50\%}$, obtaining the modified Avrami equation:

$$X = 1 - \exp\left(-0.693\left(\frac{\varepsilon - \varepsilon_{c}}{\varepsilon_{50\%}}\right)^{n}\right) \tag{46}$$

A common assumption is to consider that DRX occurs at the peak of the flow stress. Therefore, the softening induced by recrystallization can be computed by decreasing the flow stress from the peak stress to the steady-state stress, σ_{p} to σ_{s}. Thus, the fractional softening X can be expressed as follows:

$$x = \frac{\sigma_{p} - \sigma}{\sigma_{p} - \sigma_{s}} \tag{47}$$

This way, incorporating this expression into Eq. (33), the modified form of the JMAK equation for DRX is obtained:

$$X = \frac{\sigma_{p} - \sigma}{\sigma_{p} - \sigma_{s}} = -1 - \exp\left[-k\left(\frac{\varepsilon - \varepsilon_{p}}{\dot{\varepsilon}}\right)^{n}\right] \tag{48}$$

This expression can be rewritten as follows, so as to calculate the material constant k and n, by plotting lnln(1/(1-X)) - ln $(\varepsilon - \varepsilon_{p}/)$.

$$\text{lnln}\left[1/\left(1 - \frac{\sigma_{p-\sigma}}{\sigma_{p-\sigma_{s}}}\right)\right] = \ln k + n\ln\left(\frac{\varepsilon - \varepsilon_{p}}{\dot{\varepsilon}}\right) \tag{49}$$

The analysis of these two parameters about deformation conditions for martensitic stainless steels shows that while there is a clear relationship between n and Z, it is not the case for k. Momeni et al. [55,57]. The relationship between n and Z for AISI 410 steel is:

$$n = 24.442^{-0.068} \tag{50}$$

Some differences can be found in expression 41 depending on the definition of the fractional softening, X, and time transformation into deformation. Momeni et al. [52] separated the recrystallizing process into two parts: the part occurring state strain, ε_{s}. They supposed that at the peak stress $X = 0.1$, accordingly, the expression of recrystallizing time is expressed as the ratio of strain differences.

$$X|_{\varepsilon_p}^{\varepsilon_s} = 0.9 - \exp\left[-0.693\left(\frac{2(\varepsilon-\varepsilon_p)}{\varepsilon_s-\varepsilon_p}\right)^n\right] \quad (51)$$

with the same Equation for n as in Eq. (39). Other authors used Eq. (41) to calculate the progress of dynamic recrystallization fraction or fractional softening (X), considering the initial flow stress as that obtained if dynamic recovery is the only softening mechanism σ_{WH}, and the saturation flow stress σ_{sat} [58,62].

$$X_{drx} = \frac{\sigma_{drv}-\sigma}{\sigma_{sat}-\sigma} \quad (52)$$

This expression leads to the following Eq. (51) for X20Cr13 [58]:

$$X_{drx} = 1 - \exp\left(-0.2194\left(\frac{\varepsilon-\varepsilon_c}{\varepsilon_{Pp}}\right)^{2.9764}\right) \quad (53)$$

As it has been shown models based on the same equation consider different approaches for determining the parameters included in the DRX process, e.g determination of the beginning of recrystallization (peak of the flow stress in most cases), identification of maximum recrystallization, even the fractional softening is related to stress, time or strain depending on the researchers interest. The concordance between the assumption and the equations in each case has allowed researchers to obtain results with a good level of correlation.

3.3. *Baragar and McQueen constitutive equations*

Baragar proposed a constitutive relation for plain carbon and low alloy steels using the power equation as follows [91]:

$$\sigma = b + c\varepsilon^{0.4} + d\varepsilon^{0.8} + e\varepsilon^{1.2} \quad (54)$$

where b, c, d, and e are material constants. However, these constants can vary significantly depending on the deformation condition. In order to modify this relation, another experimental equation proposed by Cingara and McQueen can be used, which yields [92]:

$$\frac{\sigma}{\sigma_p} = \left[\left(\frac{\varepsilon}{\varepsilon_\rho}\right)\exp\left(1-\frac{\varepsilon}{\varepsilon_\rho}\right)\right]^C \quad (55)$$

where C is a material constant and σ_p, and ε_ρ corresponds to the peak stress and strain. Eq. (55) can be simplified if the Taylor series for the exponential function ($\exp(x) = 1+x+x^2/2!+\ldots$) is used, which results in:

$$\frac{\sigma}{\sigma_p} = \left[2.5\left(\frac{\varepsilon}{\varepsilon_p}\right) - 2\left(\frac{\varepsilon}{\varepsilon_\rho}\right)^2 + 0.5\left(\frac{\varepsilon}{\varepsilon_\rho}\right)^3\right]^C \quad (56)$$

Then, rewriting Eq. (56) and neglecting some terms for simplicity, it can take the form of Baragar's Equation as follows:

$$\sigma = \sigma_p\left[2.5\left(\frac{\varepsilon}{\varepsilon_p}\right)^C - 2\left(\frac{\varepsilon}{\varepsilon_\rho}\right)^{2C} + 0.5\left(\frac{\varepsilon}{\varepsilon_\rho}\right)^{3C}\right] \quad (57)$$

The value of C can be determined from the experimental data by taking the logarithm of both sides of Eq. (57). The calculated average value of C was 0.7. The model successfully predicted the flow curves of the material up to the steady-state region. Momeni et al. [52] also used Cingara and McQueen [92] experimental Eq. (48) to model the flow stress curve up to the peak point. They found an average value of $C = 0.47$ for the AISI 410 MSS, whose value defines the ratio between work hardening (WH) and dynamic recovery (DRV). The lower is C, the lower is the WH, or the higher is the DRV. However, it was concluded that this empirical formulation leads to a worse flow curve approximation than other phenomenological models.

3.4. *Johnson Cook (JC)*

Johnson Cook (JC) model is a physical model developed to predict the stress–strain relation for those materials subjected to high temperature, high strain rate, and large strain [93]. This model considers the material strain hardening, strain rate hardening, and thermal softening. However, one important limitation is the consideration of these material phenomena as an independent. The flow stress σ is calculated according to:

$$\sigma = (A + B\varepsilon^n)(1 + C\ln\dot{\varepsilon}^*)(1 - T^{*m}) \quad (58)$$

where A is the material yield stress at the reference strain rate and temperature, B is the strain hardening constant, ε is the plastic strain, n is the strain hardening coefficient, C is the strain rate strengthening coefficient, and m is the thermal softening coefficient. Moreover, $\dot{\varepsilon}^*$ is the dimensionless strain rate that is defined as the ratio between the actual and the reference strain rate, resulting in:

$$\varepsilon^* = \frac{\dot{\varepsilon}}{\dot{\varepsilon}_0} \quad (59)$$

where $\dot{\varepsilon}$ is the actual value of strain rate, and $\dot{\varepsilon}_0$ is the reference one. The homologous temperature T^* is calculated according to:

$$T^* = \frac{T - T_{ref}}{T_m - T_{ref}} \quad (60)$$

where T is the actual temperature (T_m) is the material's melting temperature, and T_{ref} is the reference temperature. As a result, 5 variables have to be defined to model the material behavior. One advantage is that the number of required experiments to determine their values is limited compared to other constitutive formulations. At the reference values of temperature and strain rate ($T = T_{ref}$ and $\dot{\varepsilon} = \dot{\varepsilon}_0$), Eq. (58) yields

$$\sigma = (A + B\varepsilon^n), \quad (61)$$

which after its rearrangement and by taking natural logarithm on both sides results in:

$$\ln(\sigma - A) = \ln B + n\ln\varepsilon \quad (62)$$

Then, the plot of the relation $\ln(\sigma - A)$ vs $\ln(\varepsilon)$ is used to determine both B and n by linear fitting as the intercept and slope, respectively. Similarly, at the reference temperature ($T^* = 0$), the flow softening term results in 1, and thus, Eq. (58) can be expressed as:

$$\sigma = (A + B\varepsilon^n)(1 + C\ln\dot{\varepsilon}^*) \quad (63)$$

The determination of constant C is conducted by using the flow stress at a specific strain for different strain rates. Therefore, C is calculated as the slope of $\frac{\sigma}{A+B\varepsilon^n}$ vs $\ln\dot{\varepsilon}$. Finally,

at the reference strain rate ($\dot{\varepsilon} = \dot{\varepsilon}_0$), the strain rate hardening term can be neglected, and thus, the thermal softening effect on flow stress is isolated. Then, Eq. (58) leads to

$$\sigma = (A + B\varepsilon^n)(1 - T^{*m}) \tag{64}$$

The constant material m is calculated from the slope of the plot $\ln\left(1 - \left\{\frac{\sigma}{A+B\varepsilon^n}\right\}\right)$ vs $\ln T^*$. This model presents some drawbacks reported in the literature regarding the precision of the results and the applicability to different crystal structures. Then, the main modified versions of this model are presented, indicating which material is used for their validation, and, afterward, those applied to MSS are further explained. Zhang et al. [94] included the effect of temperature on strain hardening by modifying the terms related to the thermal softening and strain hardening in the original model to predict the stress of IC10 alloy accurately. This model was used in an MSS to predict the dynamic mechanical behavior of single-phase better than the original JC.

Among the models described, both the original proposed by JC and some of the modified ones have been used for MSS. These models are generally linked to the dynamic description of the material behavior in cutting and friction stir welding processes. Zhang et al. [95] used the original JC model to describe the 4Cr13 Stainless Steel to give the foundation for finite element analysis during the cutting process. Korkmaz and Günay [96] used the original JC model to study the AISI 420 MSS machinability. A similar model was used in an FSW process for a 1Cr11Ni2W2MoV MSS leading to an accurate description of the material behavior under high strain and strain rate [48]. Krishna et al. [97] compared the predictability of the original JC model and the JC-modified model proposed by Lin et al. for a Nitrogen Alloyed Martensitic Stainless Steel. The improvement in prediction accuracy of the modified JC model was attributed to the consideration of conjugated effects of temperature and strain rate on the flow stress.

The precision of the JC model compared to other flow stress models is limited. The use of modified versions extends its use in different crystal structures and increases the precision but, in metal forming processes, the use of these models is restricted to processes at high strain rates.

3.5. *Flow stress models based on dislocation density evolution*

In the absence of DRX, Estrin and Mecking (EM) approach are valid for calculating the material flow stress. It defines a dependency of the dislocation density on plastic strain according to the following Equation [98]:

$$\frac{d\rho}{d\varepsilon} = h - r\rho, \tag{65}$$

where h is the athermal work-hardening rate, r is the rate of dynamic recovery at a particular value of strain rate, and temperature and ρ is the dislocation density. The athermal work-hardening and dynamic recovery rates can be considered independent of the applied strain. The integration of the proposed differential equation yields:

$$\sigma = \left[\sigma_{rec}^2 - \left(\sigma_{rec}^2 - \sigma_0^2\right)\exp(-r\varepsilon)\right]^{0.5} \tag{66}$$

where σ_{rec} stands for the saturation stress and σ_0 is the initial stress. The saturation stress and the initial stress are equal to $(\alpha MGb)^2(h/r)$ and $(\alpha MGb)^2\rho_0$, respectively. α is a shape factor, M is the Taylor factor (3.07 for FCC materials), G is the shear modulus, and b is the magnitude of Burguer's vector. The flow stress σ represents the imaginary stress that could be achieved without the softening effect of DRX, and thus, to account for this softening behavior, the critical strain or stress for the onset of DRX has to be calculated. After this point, the fractional softening due to DRX is subtracted from the flow stress predicted by Eq. (65).

Mirzadeh et al. [62] and Wang et al. [99] used physically-based flow stress models based on EM approach for modeling the behavior of a 17–4 PH and 2Cr11Mo1VNbN MSS, respectively. Their models reported good results up to the critical strain for the onset of DRX, and, in both cases, Avrami-type equations were used to model the softening due to DRX. Momeni et al. [100] proposed a modification of Eq. (65) by assuming that ρ_0 is almost negligible compared to the generated dislocation density during hot deformation. As a result, the flow stress can be considered as:

$$\sigma = \sigma_{rec}(1 - \exp(-r\varepsilon))^{0.5} \tag{67}$$

This assumption is also more applicable to low SFE materials such as austenitic steels characterized by a sluggish DRV process. However, it was applied in the calculation of σ_{rec} and r satisfactorily for martensitic stainless steel such as AISI 410, which is considered a high SFE material [9]. Safara et al. [101] proposed an alternative description of flow stress of an MSS based on a dislocation density evolution approach based on Taylor equation, used previously in a wide range of crystalline materials and alloys [102].

$$\sigma_i = \sigma_0 + \alpha MGb\rho_i^{0.5} \tag{68}$$

where the index (i) allows distinguishing between the calculation of stress and the corresponding dislocation density for deformed and recrystallized states, once both states are calculated, the total flow stress is calculated according to the mixture law and the dynamically recrystallized fraction. The flow stress predictions matched adequately with the experimental results.

Flow stress models based on dislocation density present the advantage of being based on physical relations, and consequently more reliable. However, they are more difficult to adjust given the higher number of experiments required while the precision obtained is comparable to other phenomenological relations. This fact explains why their use is not widely extended in the description of material flow stress.

3.6. *Material processing mapping*

Material processing maps were developed by Prasad et al. [103] based on the dynamic material model concept. In the case of MSS, they have been widely used in both the description of the microstructure evolution during hot deformation and the definition of the optimum material hot deformation conditions [86,87].

The dynamic materials model (DMM) considers the workpiece as a dissipator during hot material deformation, which shows a dynamic and nonlinear response in a non-equilibrium manner with subsequent irreversible changes [71]. The power (P) absorbed by the workpiece during hot working can be divided into two complementary parts: the dissipative content G and the dissipative co-content J. G represents the plastic deformation with the generation of heat, while J denotes the energy for metallurgical reconstitution process, such as DRV, DRX, flow localization, phase transition and shear band formation [104]. The power partitioning is defined by the constitutive Equation of plastic flow, specifically by the strain rate sensitivity parameter, m. In order to quantify the amount of power dissipation for microstructural reconstitution, it is possible to normalize the J-co content with input power. When this parameter is compared to an ideal power dissipater (m = 1), it yields the efficiency of power dissipation (η), a dimensionless parameter. Then, the total power dissipated can be calculated according to:

$$P = \sigma\dot{\varepsilon} = \int_0^{\varepsilon} \sigma \, d\dot{\varepsilon} + \int_0^{\sigma} \dot{\varepsilon} \, d\sigma = G + J \tag{69}$$

The flow stress, in the simplest form (constant strain and temperature), can be given by:

$$\sigma = k\dot{\varepsilon}^m \tag{70}$$

where σ is the flow stress, $\dot{\varepsilon}$ is the strain rate, m is the material strain rate sensitivity, and k is the material constant. From Eq. (69) and Eq. (70), the power partitioning between G and J is calculated as:

$$\frac{dJ}{dG} = \frac{\dot{\varepsilon}\, d\sigma}{\sigma\, d\dot{\varepsilon}} = \frac{d(\ln \sigma)}{d(\ln \dot{\varepsilon})} = m \text{ (strain rate sensitivity parameter)} \tag{71}$$

Then, from Eqs. (68)–(70), at a given temperature and strain, the dissipative co-content J yields:

$$J = mG = m(\sigma\dot{\varepsilon} - J) = \frac{m}{m+1}\sigma\dot{\varepsilon} \tag{72}$$

As previously stated, in the case of an ideal dissipator, $m = 1$ and G equals J. By using this definition, the dimensionless efficiency of power dissipation η results in:

$$\eta = \frac{J}{J_{max}} = \frac{m\bar{\sigma}\dot{\varepsilon}/(m+1)}{\bar{\sigma}\dot{\varepsilon}/2} = \frac{2m}{m+1} \tag{73}$$

where $J_{max} = \frac{\bar{\sigma}\dot{\varepsilon}}{2}$ when $m = 1$. In material processing, unless deformation is conducted on the maximum efficiency of power dissipation regions, it may result in instabilities. The instability during the hot deformation of materials can occur in flow localization, adiabatic shear bands, kink bands, dynamic strain aging (Luder's bands), and flow rotation. The determination of those regions in which material deformation leads to microstructural instability is based on the maximum rate of entropy production [105]. The instability parameter, $\xi(\varepsilon)$, can be used to identify those regions according to:

$$\xi(\dot{\varepsilon}) = \partial \frac{\ln[m/(m+1)]}{\partial \ln \dot{\varepsilon}} + m < 0 \tag{74}$$

Therefore, material instability occurs when the value of the instability parameter $\xi(\varepsilon)$ is negative. However, it is vital to notice that the efficiency of power dissipation (η) given in Eq. (73) is valid only when the flow stress (σ) - strain rate (ε) curve, at any strain and temperature, follows the power-law presented in Eq. (70). Consequently, the parameter m is independent of (ε), and thus, the flow instability condition reduces to $m < 0$ [106].

In the reviewed literature concerning the development of material processing maps for MSS, many authors used the power law (Eq. (70)) and the flow instability criterion as $m < 0$. Momeni et al. [51] identified two instability regions in a 410 MSS; any experimental observation of these regions was performed. Zou et al. [87] analyzed a 00Cr13Ni5Mo2 super martensitic steel and identified flow localization and low level of dynamic recovery are the main reasons for instability occurring. These regions were examined experimentally using optical microscopy (OM) and scanning electron microscopy (SEM). Kishor et al. [76] revealed localized flow structure and shear bands due to the absence of steady-state behavior corresponding to the instability region (900 °C, 10 s^{-1}) for a 13Cr–4Ni MSS. Chegini et al. [76] based on the processing maps, used OM to investigate an instability region for the AISI 414 at the temperature range of 950–1150 °C, strain rate range of 0.001–1 s^{-1}, at a strain of 0.4. Zhou et al. [86] developed the processing maps for a 05Cr17Ni4Cu4Nb MSS and performed optically and SEM observations in the predicted instability region, which showed intergranular cracks and voids, which may lead to the unstable deformation. Zhao et al. [84] analyzed the processing of a 1Cr12Ni2Mo2WVNb steel using DMM model and optical and SEM observations. Two instability domains were found under the strains of 0.3, 0.4, 0.5, and 0.6. The deformation temperature of 950 °C should be avoided, given that deformed twins are found, which are associated with a low DRV level that suppresses the grain deformation and grain boundary sliding.

An alternative definition of the material strain rate sensitivity was followed by assuming that at a given strain and deformation temperature, the relationship between true stress and strain rate can be expressed through a cubic spline fit [107]. This relationship was established according to:

$$\log \sigma = a + b \log \dot{\varepsilon} + b_1(\log \dot{\varepsilon})^2 + b_2(\log \dot{\varepsilon})^3 \tag{75}$$

If the partial differential is taken from both sides of Eq. (75), m results in:

$$m = b + 2b_1 \log \dot{\varepsilon} + 3b_2(\log \dot{\varepsilon})^2 \tag{76}$$

Ren et al. [80] followed this approach to develop the processing maps of a 420 MSS and identified three possible instability regions. In addition, it was noted that critical strain could be used to determine whether the unstable flow occurs at relatively high deformation temperatures. Li et al. [77] analyzed the processing of a Nitrogen-Bearing MSS. The microstructure in the unstable region was analyzed by TEM, which manifested the deformation twins and the bands of flow localization (Fig. 3). The twins' boundaries were associated with dislocations motion inhibition, which may cause dislocation pile-ups and, in turn, can result in stress concentration and voids, and microcrack formation.

In the case of complicated alloy systems, which do not obey the power law, the use of the previously discussed flow

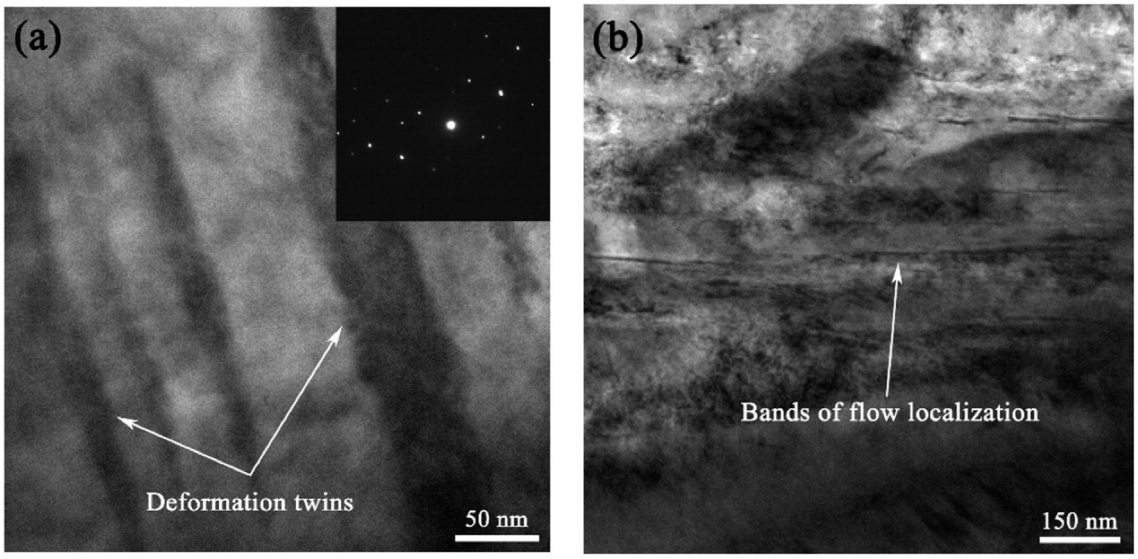

Fig. 3 – TEM images of the Nitrogen-Bearing MSS at the deformation condition of 1000 °C and 0.01 s^{-1} [77].

instability condition might lead to errors. Indeed, it has been reported that the strain rate sensitivity parameter is only independent of the deformation temperature and strain rate on pure metals or low alloys [108], while it is dependent on temperature and strain rate in the case of complex alloys [109]. Hence, Murty et al. [110] proposed an alternative criterion, valid for any kind of flow stress–strain behavior. The proposed condition for flow instability is calculated according to:

$$2m < \eta \tag{77}$$

The ideal plastic flow consists of the dissipation of half of the power in terms of material flow and the other half, as power dissipated as viscous heat. However, some materials are not sensitive to strain rate, which leads to $m = 0$ and thus, $J = 0$. In this case, $G = P$ and all the dissipation are conducted in terms of heat, which would lead to plastic instability in the form of flow shear bands. Hence, the efficiency of power dissipation η results in:

$$J = 0 \Rightarrow \eta = 0 \tag{78}$$

and thus, for any kind of flow stress distribution, the new condition for metallurgical instability can be defined as:

$$2m < \eta \leq 0 \tag{79}$$

As a result, the flow is stable when the efficiency of power dissipation value complies with $0 < \eta < 2m$. In addition, from theoretical considerations of the maximum power dissipation rate, the range of m values yields $0 < m \leq 1$. If the stress–strain curve complies with the power law, then:

$$\eta = \frac{2m}{(m+1)} \tag{80}$$

and thus, the efficiency of power dissipation is lower than $2m$ (for $0 < m \leq 1$). Therefore, the material flow can be considered stable. Anoop et al. [71] used the previously described instability criterion for developing the power dissipation efficiency map of 12Cr–10Ni steel. Fig. 4 shows the power efficiency map at a strain of 0.5 and color EBSD IPF (inverse pole figure) corresponding to various regions of power dissipation efficiency. The high-efficiency areas are located at lower strain rates and higher temperatures, while the lower efficiency ones lie in the low temperature and high strain rate regime.

In addition, a wide, stable window in the temperature range 1223–1323 K (950°–1050 °C) and strain rates of 0.001–0.1 s^{-1} were identified from the instability contour map. At these working conditions, the IPF showed fine grains and grain boundary measurements by EBSD, indicating a high angle boundary fraction of 89.7 and 85%, respectively.

The same instability criterion was used to define the hot processing maps of the FV520B MSS by Huang and Fen [65]. The high values of power dissipation efficiency are identified at temperatures above 1050 °C and low strain rates ($\dot{\varepsilon}$ <0.2 s^{-1}). The unstable regions are present at high strain rates ($\dot{\varepsilon}$ >0.1 s^{-1}) and low temperatures. In addition, the unstable region is higher; the higher is the strain.

From the reviewed literature, it can be stated that processing maps give insightful information about the optimum deformation conditions and microstructure evolution. However, many works use the power law and flow instability criterions that might lead to errors, given that complex alloys such as MSS would not obey the power law, and thus strain sensitivity parameter is dependent on temperature and strain rate. However, the use of alternative criterions, such as the one proposed by Murty et al. [99], is proved to give an accurate description of the unstable working conditions of MSS.

3.7. *Finite element analysis of DRX in MSS*

FEM codes are commonly used as a macro scale in the field of hot bulk metal forming. The FE simulation provides comprehensive information about the material macroscopic behavior under large deformations and thermal fluctuations, characteristic of

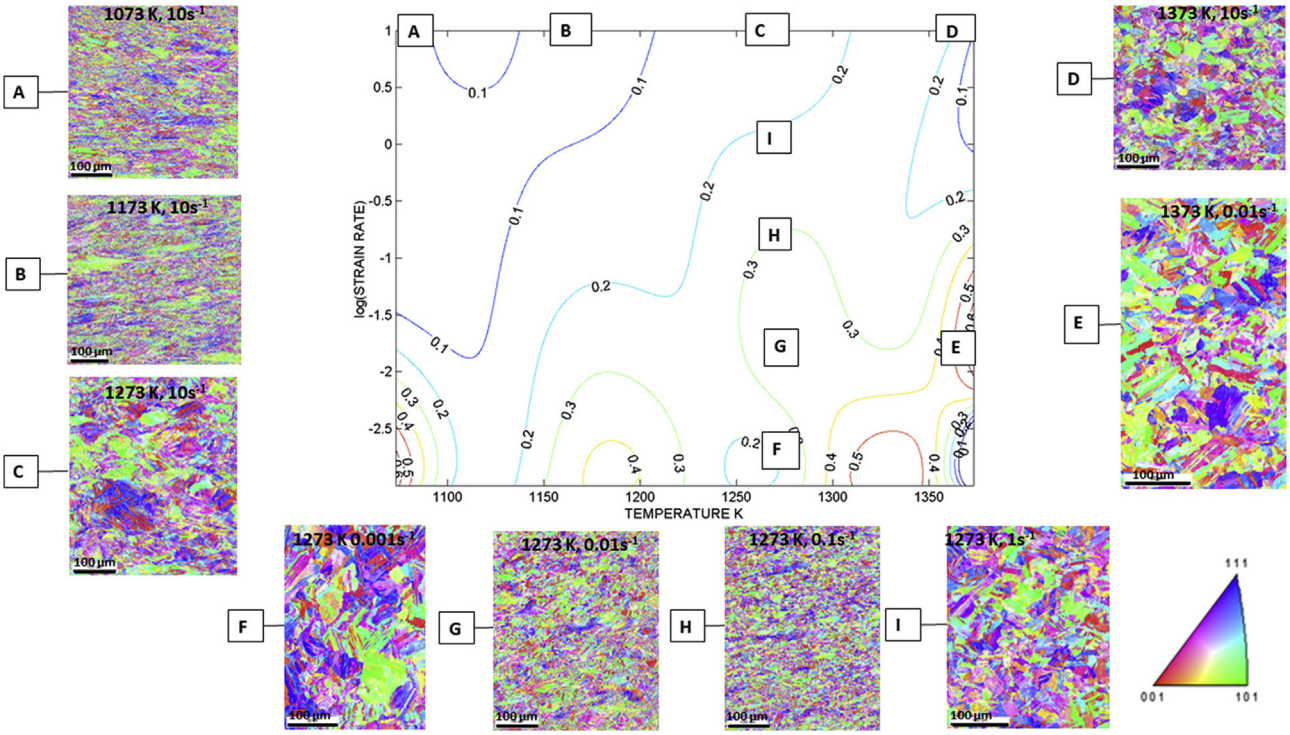

Fig. 4 – Contour map of the efficiency of power dissipation for a 12Cr–10Ni MSS at a strain of 0.5 with EBSD IPF maps of deformed specimens [71].

metal forming processes. This type of software has become widespread since it is difficult to obtain analytical solutions in processes in which high nonlinearities are present, the material exhibits anisotropic behavior, and irregular-shaped surfaces are put under changing contact. Therefore, initially, FEM was applied in metal forming processes to define the material temperature evolution and the stress and strain distributions during its processing. Nevertheless, the use of FEM in metal forming is not limited to the analysis of material macroscopic behavior. The use of finite element modeling and simulation of microstructure evolution is one of the most important ways to improve the quality of the final products. In hot forming processes, dynamic recrystallization (DRX), metadynamic recrystallization (MDRX), and static recrystallization (SRX) affect the final grain size distribution. In grain refinement-based processes, it is especially interesting to reproduce the evolution of the austenitic grain size mathematically during its processing. In the previous section, several mathematical models for predicting DRX and kinetics of recrystallization have been introduced. In order to test the validity of these mathematical descriptions, a standard procedure is the development of finite element models (FEM) of the compression test [111]. These FEM allow testing the predicted DRX fractions and grain size under different deformation conditions and, after that, these results can be compared to the experimental observations to analyze the quality of predictions.

Li et al. [113] developed a constitutive model based on the FEM approach for the DRV curve and Avrami equation to define the volume fraction recrystallized. They analyzed the effect of the temperature and strain rate fluctuations on the DRX prediction. In addition, the dynamic recrystallized grain size was associated with the Zener-Hollomon parameter value according to the work of Sellars et al. [114], but the results of the model in terms of grain size were not compared to experimental observations. Similarly, Ji et al. [112] developed the formulation for the DRX volume fraction using the Johnson–Mehl–Avrami–Kolmogorov (JMAK) equation for a heat resistant steel, and the dynamic recrystallized grain evolution was also made dependent on Z.

In this case, the results of DRX volume fraction and average simulated grain size were compared to experimental observations made by EBSD. Regarding the DRX volume fraction, when T increases, the number of low-angle grain boundaries (LAGBs) decreases while the number of high-angle grain boundaries (HAGBs) increases. It points out that the DRX volume fraction increases when T increases. The experimental results of average grain size measured by EBSD showed slightly lower values than the predicted ones. In Fig. 5, the predicted grain size and the SEM experimental observations for different degrees of deformation are shown. Baron et al. [115] developed the description of the constitutive behavior of a high-strength martensitic steel MS-W 1200 for finite element simulations. The constitutive behavior was based on Taylor relation, but based on the previous work of Herman et al. [116], the influence of the solid solution hardening on the saturation stress and the carbon content influence on the recovery parameter was considered. The kinetics of recrystallization followed the JMAK equation, which was dependent on strain rather than time. The flow stress was calculated using the mixture law by considering the flow stresses of the two individual phases (deformed and recrystallized), while the resulting austenitic grain size was also calculated using the mixing rule. The relation between the

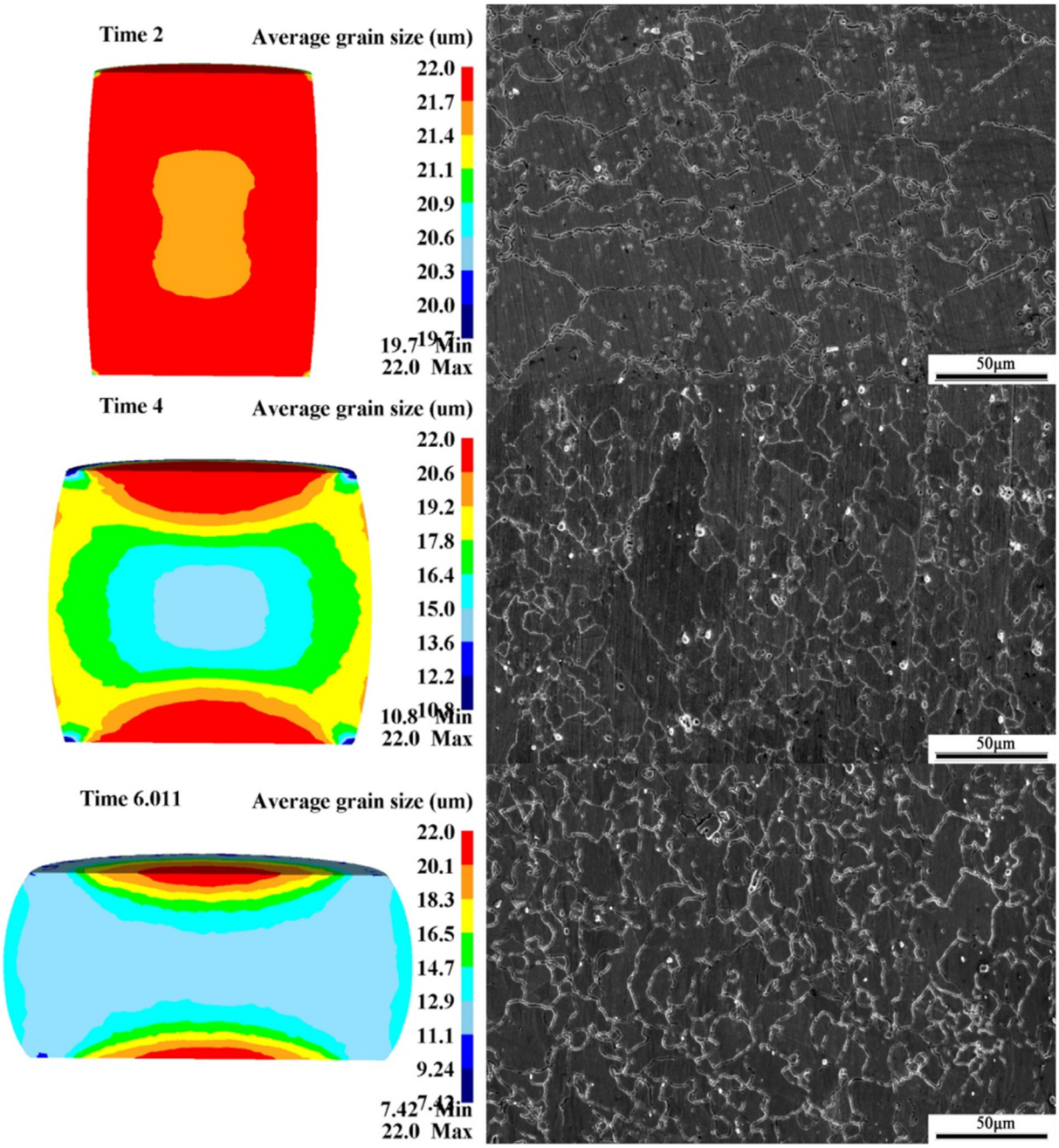

Fig. 5 – Predicted and observed grain size at different time lapses during the compression test [112].

initial microstructure and the newly formed grain size followed a Hall-Petch-like relation. The simulated grain size distribution was provided, but there was no experimental validation; the model was tested by comparing the force-stroke values of the simulation and experiment.

Chen et al. [117] developed a multi-physical formulation for an X20Cr13 MSS, which reproduced the material's dynamic, metadynamic and static recrystallizations and introduced this material model in a commercial FE software using a subroutine. The DRX volume fraction was calculated using an Avrami equation, while the dynamic recrystallized grain size was determined using a power-law relation based on the Z parameter. First, the material formulation was tested using a FE simulation of a compression test, compared to the optical microstructure observations of the material at different deformation conditions. Finally, the hot forging process of a turbine blade was simulated. The average grain size distributions at different strokes during the forging process were analyzed. An industrial experiment was carried out to analyze and compare the predicted grain size distribution with the actual process using optical microstructure observations. In Fig. 6, the average grain size distribution during the forging process of the turbine blade, at different press strokes, is provided.

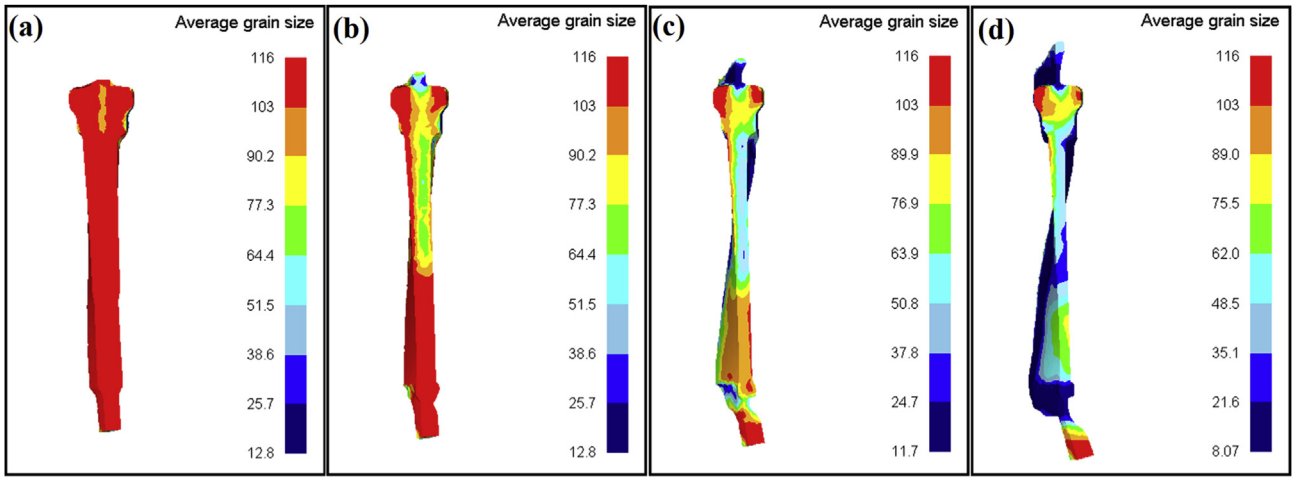

Fig. 6 – The distribution of average grain size during hot deformation at the stroke of a 48.8 mm, b 58.8 mm, c 68.1 mm, and d 72.6 mm [117].

The reviewed papers put into evidence that finite element simulations provided insightful information about the material microstructure during its processing. In the field of MSS, very few contributions deal with this topic, even though it has been shown that they can provide precious information on the dynamic recrystallization of the material in hot metal forming processes. In the hot compression tests, the prediction capacity is good in DRX volume fraction and grain size distribution, but it is related to the relatively homogeneous and constant deformation conditions during these tests. In hot metal forming processes under not controlled deformation conditions, the predictability of FE simulations is still to be assessed because the mathematical constitutive formulations describe the material behavior under steady deformation conditions. It may lead to errors in the DRX volume fraction or average grain size predictions.

4. Modelling of microstructure evolution during dynamic recrystallization of MSS

In recent years, computational materials engineering (CME) has appeared as an emerging interdisciplinary subject [118]. CME has attracted more and more attention. In the near past, engineers were adopted various forms of computer-aided design (CAD) by the metal forming industry to evaluate materials behaviour during manufacturing processes [119]. CME integrates materials selection, production, and process optimization and focuses on material microstructure evolution on the manufacturing process and final component performance during production processing [120]. In CME, the initial microstructure information is used as the input of a simulation tool (computer software) to simulate the deformation process at a macroscopic scale and the corresponding microstructure evolution [121]. Due to the simulation results, the material performance analysis and the optimization of the manufacturing process are carried out [122]. The other point from the CME output result is selecting the raw materials or composition design for various products and investigating the producibility of new materials [123]. Even it could be predicted the behaviour of a specific material in a specific manufacturing process that has never been used in such a process before [124]. At the new scope of CME, it could be a predictable load bearing of products concerning microstructure. CME means quantitatively describing the relationship between material microstructure information, processing technology, and product performance. In the first step, the CME needs to simulate the evolutionary behaviour of material microstructure accurately [121]. This step is used in various manufacturing processes under different measurement scales. The primary research tool for different measurement scales analysis of manufacturing processes by CME is the multi-scale simulation. The multi-scale simulation technique mainly includes five different types [[125–127]]:

(I) Finite element method (FEM) and finite volume method (FVM): These methods are employed in the simulation of the macroscopic behaviour of materials during plastic deformation.
(II) Crystal plastic mechanics (CPM): simulates the deformation texture in cold and hot situations.
(III) Cellular automata (CA), Monte Carlo (MC) and phase-field (PF) methods: These are widely used in the simulation of the recrystallization nucleation and growth during plastic deformation or thermal processes (heat treatment and welding).
(IV) Molecular dynamics (MD): is used to predict the dynamic properties of nano-materials.
(V) Quantum mechanics of first principles are employed to study the energetic and electronic levels.

4.1. *Finite element modelling in microscale*

Dynamic recrystallization (DRX), as the effective mechanism of microstructure evolution, is the primary approach for grain refinement under thermo-mechanical plastic deformation of MSS and other metals. Usually, DRX nucleation and growth occur in metals with high and low stacking fault energy (SFE) [128]. As discussed before, the DRX phenomenon has a multi-

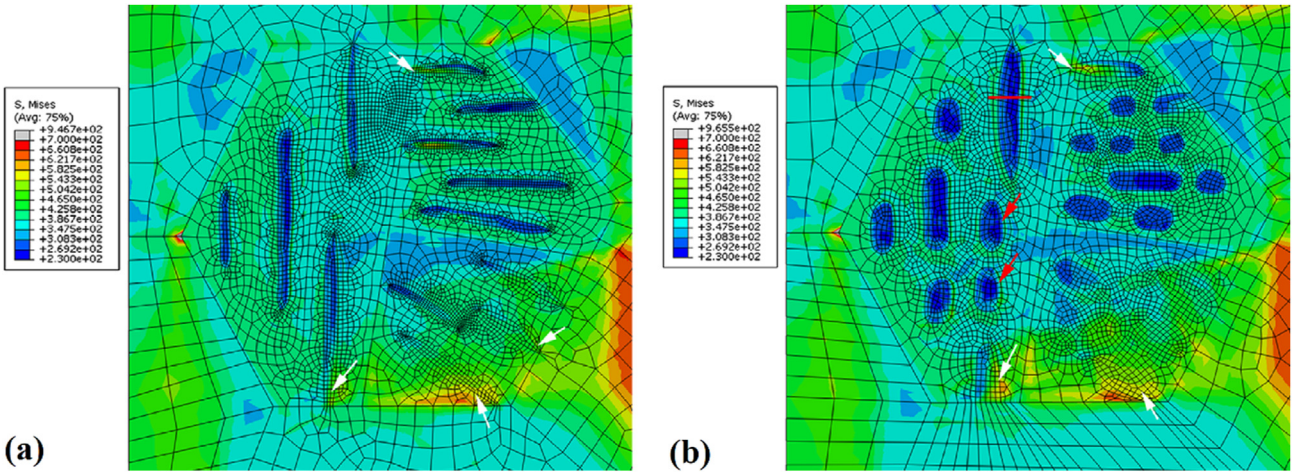

Fig. 7 – The von Mises stress field of the MSS after 4% engineering strain: (a) elongated of reversed austenite and (b) non-elongated of reversed austenite [136].

scale nature consisting of impurities, precipitation, dislocation motion, and grain boundary (GB) movement [129]. Theoretical models for the prediction or analysis of DRX include multipart mathematical calculations and many assumptions [130]. The lack of visualization from mathematical models do not reasonably describe the physical processes and makes it hard to understand the microstructure phenomenon [131]. Various types of mathematical models and their results were discussed in the previous sections. These days, with the rapid growth of computer modelling and numerical methods, it is possible to develop a processor model to simulate the DRX process. The thermodynamic and DRX evolution equations help to understand microstructure changes during hot forming process of metallic materials. Simulation of microstructure changes during hot deformation provides the feasibility of studying more advanced and complex materials. With this type of simulation, visualization of metallic materials behaviour prediction is possible under various processing conditions [132].

Generally, the plasticity finite element method (CPFEM) simulates crystallographic orientation or plastic deformation [133]. This model has been widely used for polycrystalline materials at grain scale to simulate heterogeneous deformation behaviours [134]. The CPFEM results of the single-phase crystal structure like BCC, FCC, or HCP, have been also implemented to predict mechanical properties of metallic materials on a bulk scale. Recently, the CPFEM extended was used to multiphase steel. Within the available literature, just one research deals with CPFEM simulation of MSS under micromechanical loading. A developed crystal plasticity model was implemented to study the micromechanical behaviour of the reversed austenite in 13Cr4Ni steel during the mechanical loading. The effect of the structural characteristics on the stability of the reversed austenite was the primary concern modelling [135].

So far, no research has been published in CPFEM of MSS hot deformation. However, among the reported investigations, Wang et al. [136] reported the effect of the structural characteristics on the stability of the reverted austenite in 13%Cr MSS during warm deformation. In their study, the samples heated up to 630 °C. Their study focuses mainly on the stress and strain evolution during the small straining deformation without considering the austenite to martensite phase transformation. According to the observed lath martensite structure in the experimental procedure, the calculation domain was considered, and the central prior austenite grain was divided into three packets, and each packet contains only one martensite block. They considered two samples with 10% and 20% fractions of the austenite at the martensite lath boundaries. Fig. 7a and b demonstrate local von Mises equivalent stress distribution simulation results after 4% engineering strain at the samples. The CPFEM simulation results show that the local stress is heterogeneous at the microscopic level when the grain orientations and the activated slip systems are considered. The stress in the reversed austenite is lower than that in the surrounding martensite matrix. The activation of slip systems in MSS decreases the stress at the phase boundaries and enhances the mechanical stability of the reversed austenite during the deformation [135].

4.2. *Monte carlo modelling in microscale*

The following five categories have been frequently used in the modelling of microstructure evolution in DRX processes. These types are discrete or continuous mesoscale methodologies that consist of PF (phase field), LS (level-set), MC (Monte Carlo), VM (vertex) and CA (cellular automaton) methods. These methods can not only meaningfully reproduce the evolution of microstructures, but can also predict microstructure characteristics [137].

LS and PF methods use continuous functions to simulate. The continuous function allows LS and PF methods to direct the representation of grain boundaries and curvatures. The grain boundaries and curvatures are challenging to achieve with other mesoscale methodologies. However, the use of both LS and PF models is limited. Both can be used in homogeneous deformation and, compared to other mesoscale methodologies, require more computational time. Hitherto, no report has been submitted on the simulation of MSS behaviour using LS and PF methods.

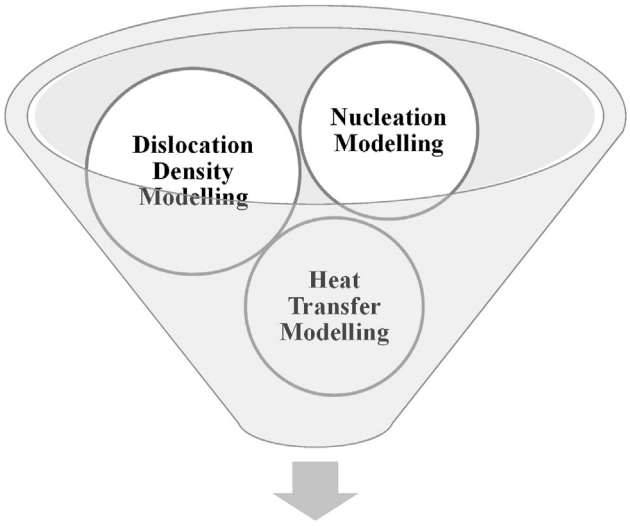

Fig. 8 – The MC simulation requirements.

In the available literature, the simulation of recrystallization nucleation and growth processes of metallic materials is mainly handled by using discrete methods like vertex, CA and MC methods. In the MC method, the grain topography is discretized into polygon lattice points. All grid points have an orientation; randomly select a grid point and make a positional transformation. Transformation probability is related to the freedom energy inside the considered domain (system). The MC method is a simple numerical model and moderately easy to implement. In this method, the calculation is high-speed, the change of grain size information can be obtained, and the evolution of grain morphology can also be observed. For these reasons, the mechanism of grain growth can be followed by the MC simulation results. Analogous to all simulation procedures, the MC has disadvantages, such as:

1 There is no random transformation or deterministic rule in this approach
2 The MC results do not reflect the mechanism of the grain boundary change.
3 The grain growth index result from MC is different from the theoretical grain growth index.

For the MC simulation, it is required to import a couple of sub-models. These sub-models and simulation steps are depicted in Fig. 8.

4.2.1. *Nucleation modelling during recrystallization*

For initiation of DRX, a critical dislocation density is necessary. During high strain rates, in the hot deformation of MSS, the DRX nucleus forms at existing grain boundaries [138]. During DRX, the concurrent deformation reduces the driving force (stored energy differences) at grains boundaries that affect high-angle boundaries migration [139]. At the first step for prediction of nucleation during recrystallization, the net free energy must be calculated as [139]:

$$\Delta G(r) = -\frac{4}{3}\pi r^3 \frac{\tau}{r}\int_0^r [\rho_{d0} - \rho_d(x)]dx + 4\pi r^2 \gamma_{GB} \tag{81}$$

In Eq. (81), the ρ_{d0}, τ, γ_{GB}, $\rho_d(x)$ and r represents dislocation energy at initial step, mean dislocation energy per unit of length, energy of grain boundary per unit area, increased dislocation density, and radius of nucleus, respectively. The net free energy may be maximized to obtain the following critical nucleation condition [140]:

$$r_{cr}\gamma\left[\frac{\rho_s}{3}tanh\left(2\frac{M'}{m}\frac{\rho_s}{\rho_{d0}}r_{cr}\right) - \rho_{d0}\right] + \left(\frac{\tau\rho_{d0}m}{3M'}\right)ln\left[cosh\left(2\frac{M'}{m}\frac{\rho_s}{\rho_{d0}}r_{cr}\right) \times\right] + 2\gamma_{GB} = 0 \tag{82}$$

M', m and ρ_s, respectively represents mobility of recovery, HAGB mobility, and the density of stationary dislocation. The velocity of a GB during DRX may be expressed as [141]:

$$v = m\Delta P = m(\tau\Delta\rho_d - P_\tau)P_s \tag{83}$$

f_p represent the grain's boundary slip plane as a function of time and is defined as [142]:

$$f_p(t) = \pi\left(r_{cr} + \int_{t_{cr}}^{t} v(t)\right)^2 - f_{cr} = \pi\left[\left(\int_{t_{cr}}^{t} v(t)\right)^2 + 2r_{cr}\int_{t_{cr}}^{t} v(t)dt\right] \tag{84}$$

f_{cr} is defined as the cross-sectional area of a critical nucleus. The number of potential annihilated nuclei can be presented as [94–96]:

$$\varnothing(t) = \frac{f_p(t)}{\pi r_{cr}^2}\left(\int_{t_{cr}}^{t}\frac{v(t)}{r_{cr}}dt\right)^2 + 2\int_{t_{cr}}^{t}\frac{v(t)}{r_{cr}}dt \tag{85}$$

The number of recrystallized nuclei derived from the following Eqs, [94–96]:

$$\Theta(t) = \int_{t_{cr}}^{t}\Theta_\infty(t')\frac{m\tau\rho_{cr}}{d_{GB}}C_m dt \tag{86}$$

4.2.2. *Dislocation density model*

The average dislocation density of MSS is increased during hot deformation. Dislocation density is described by Kocks–Mecking model [143]. In Kocks–Mecking model, the flow stress is proportional to the square root of total dislocation density, which can be defined as [143]:

$$\sigma = M\alpha Gb\sqrt{\rho_d} \tag{87}$$

ρ_d known as average density of dislocations, M is Taylor factor, α represents the dislocation interaction term and has a value of 0.5 for most metals. B presents Burger's Vector and G is the shear modulus. The stored energy is related to the dislocation density and strain, as defined [144]:

$$H = \alpha Gb^2\rho_d = \frac{\alpha GbM\varepsilon}{d}\left(\frac{1}{\alpha_s} + C\right) \tag{88}$$

α_S and C are materials constant, ε and d are strain and grain size, respectively. The dislocation density evolution during deformation in the hardening regime of the flow stress is

controlled by the balance between dislocation generations and the removal of dislocations due to annihilation. The differential equation which describes the evolution of dislocation density is [145]:

$$\frac{d\rho_d}{d\varepsilon}=\frac{1}{bl}-\left[k_{20}\left[\frac{\dot{\varepsilon}}{\dot{\varepsilon}_0^*}exp\left(-\frac{Q_s}{RT}\right)\right]^{\frac{1}{n}}\right]\rho_d \tag{89}$$

The l is the mean free path for dislocation and the equation for the l in the model is given by [146,147]:

$$l=\beta\left(\dot{\varepsilon}\,exp\left(\frac{Q_d}{RT}\right)\right)^{-q} \tag{90}$$

4.2.3. *Heat transfer model*

To correctly model the microstructural evolution prediction, it is essential to reproduce the transient temperature distribution of the workpiece during hot forming. This way, the multidimensional temperature distribution can be modelled according to [38,148,149]:

$$\rho_m C_p\frac{\partial T}{\partial t}=k\left(\frac{\partial^2 T}{\partial x^2}+\frac{\partial^2 T}{\partial y^2}+\frac{\partial^2 T}{\partial z^2}\right)+\dot{q} \tag{91}$$

In Eq. (91), the $\dot{q}$ is the internal heat generation equation, and it consists on the heat power generated by plastic deformation and friction at the workpiece–tool interface during hot forming. The equation of $\dot{q}$ could be different for various forming process and hot stamping test. In general, the heat generation by plastic deformation is presented by [38,148,149]:

$$\dot{q}=\eta\sigma\dot{\varepsilon} \tag{92}$$

The effective stress, strain rate and efficacy factor are incloded in Eq. (92), that written by σ, $\dot{\varepsilon}$ and η, respectively.

4.2.4. *Monte Carlo steps*

In the MC method, a continuum microstructure is mapped onto a two-dimensional square lattice system. In this simulation procedure, each lattice site is assigned a number (SI) corresponding to the grain orientation in which it is embedded. Lattice sites adjacent to sites with different grain orientations are regarded as being separated by a grain boundary, whereas a site surrounded by sites with the same orientation is in the grain interior. To avoid the singularity of edges, periodic grain boundary conditions are used. Stored energy and local dislocation density are assigned to each site to account for work-hardening within the grains. The total energy of the system is given by [150–153]:

$$E=\frac{J}{2}\sum_{i=1}^{N}\sum_{j=1}^{M}\left(1-\delta_{s_i s_j}\right)+\sum_{i=1}^{N}H_{s_i} \tag{93}$$

In Eq. (93), J is a constant, S_i and S_j are presents the orientation number of i^{th} site and its neighbour (j). The δ is Kronecker delta. During MC simulation, grain boundary energy is assumed to have an isotropic distribution. The boundary motion's kinetics is simulated by the MC method, in which a lattice site is visited in random order. If the visited site is not recrystallized during the simulation, one of its nearest neighbour sites is selected randomly. If the selected neighbour site is recrystallized, then the visited site can change its orientation to the selected neighbour site if the change in energy associated with the change in orientation is lower than or equal to zero. Though, if the change in energy is greater than zero, the reorientation is accepted with a probability [150–153]:

$$P=\begin{cases}1 & if \quad \Delta E\le 0\\ exp\dfrac{-\Delta E}{\beta T} & if\ \Delta\ge 0\end{cases} \tag{94}$$

β is Boltzmann constant and T presents absolute temperature. Thus, successful transitions at the grain boundaries correspond to boundary migration. An original site can change orientations to either another orientation (grain growth) or a recrystallized orientation during the microstructure evolution. A recrystallized orientation may be reoriented to other recrystallized orientations. In the MC, the unit of time is defined as one step (MCS) per site, corresponding to N reorientation attempts [137]. The N is the total number of sites in the lattice system [154]. The recrystallized grains nucleation is achieved by adding new grains to the microstructure at randomly chosen positions in regular intervals. Each embryonic grain consists of four sites for a square lattice system with a new orientation from a different range of integers and stored energy of zero [150–153]. Hore et al. [155] used the MC method to simulate TIRP steel microstructure evolution during the hot strip rolling process. The simulation results show that during hot working, the recrystallized grains grow in isolation and, as time proceeds, impingement of the growing grains begins to occur. Lastly, the recrystallized grains are surrounded by other recrystallized grains (Fig. 9a). At the final stage, recrystallization proceeds only in a small fraction of the un-recrystallized area, and the predominant growth process changes to grain growth. During the isolated growth, the recrystallized grains remain circular with approximately the same radius. The boundaries are somewhat irregular, and small regions of the un-recrystallized matrix are sometimes trapped behind the recrystallized grains. Fig. 9b shows the MC simulated microstructures at 1, 10, and 100s^{-1} strain rates, respectively. The operation temperature and strain were 850 °C and 0.5. Their model had fair agreements with experimental results. As depicted in Fig. 9b, the recrystallized grain size decreases with increasing strain rate. The MC simulated microstructure for different deformation temperatures, at 1s^{-1} strain rate and 0.5 strain, are depicted in Fig. 9b. The MC method simulated the mean size of the recrystallized grains that increases when the temperature is raised from 900 °C to 1100 °C.

4.3. *Cellular automaton method*

Inherent shortcomings, such as determining the apex driving force equation and vertex equation, have restricted using VM. CA method is relatively flexible and effective in the modelling of DRX in comparison with other modelling methods [156,157]. CA model has become a helpful tool for studying DRX behaviour during various metal forming processes for its advantages. With CA results such as the information of the dimension, geometry, distribution, and texture of the grains can be obtained [23]. The below list shows the advantages of CA:

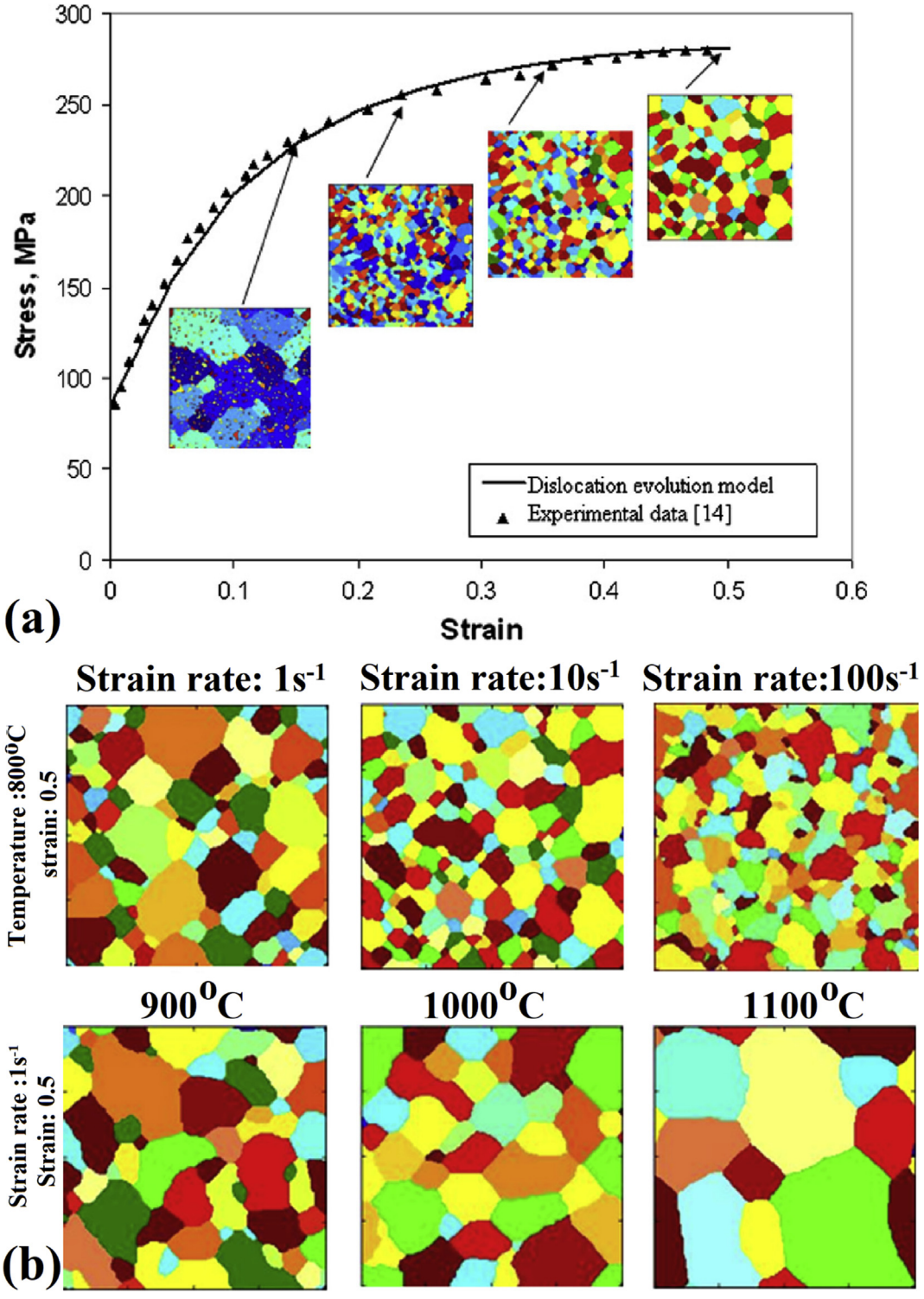

Fig. 9 – (a) The dislocation evolution model by MC. The grain growth modelling by MC method.

I. Each interval step updates the variable values simultaneously for all cells according to CA rules, depending on the system's physical model [158].
II. CA can implement discrete methods and simple local rules to describe complex physical phenomena and morphologies resulting from local interactions [27].
III. Curvature and thermodynamic-driven mechanisms and energy dissipation mechanisms are in local transformation rules in CA. These rules can more realistically reflect the physical process of grain boundaries migration in the CA method [159].

In the CA method, the complex systems are decomposed into a finite number of cells, and the complex system is described with discrete-time and space by probability transformation rules for cells [67]. Also, the time is discretized into

Table 3 – Various of dislocation density models in MC.

Model Name	Equation	Parameter names	Reference
KM	$\frac{d\rho_{i,j}}{d\varepsilon} = K_1\sqrt{\rho_{i,j}} - K_2\rho_{i,j}$	K1 = work hardening coefficient K2 = dynamic softening coefficient	[143]
EM	$\frac{d\rho}{d\varepsilon} = r.\left(\frac{\sigma_{sat}}{\alpha\mu b}\right)^2 - r\rho$ $\mu = \mu_0\left(1 - 0.91 \times \frac{T-300}{T_m}\right)$	h = work hardening coefficient r = dynamic softening coefficient σsat = saturation stress α = coefficient of the interaction of material dislocations b = Burger's vector μ = shear modulus Tm = melting temperature	[98]

time steps with a specific interval. Then the possible states of each cell are divided into a finite number of separate states. The state change of the cell at a particular time step is realized, rendering specific evolution rules. The transformation is synchronized with each cell of the system over time. Consequently, the state of a cell is affected by the conditions of the neighbouring cells. At the same time, it also affects the states of neighbouring cells.

A CA model consists of the following components [23,160]:

I. Cells (elements) are the essential component and distribute over discrete lattice points of 1-dimensional (1D), 2-dimensional (2D), or multi-dimensional Euclidean space. Frequently cell forms are triangular, quadrilateral, and hexagonal in 2D, hexahedron, and tetrakaidecahedron in 3-dimensions (3D).
II. Cellular state. In CA, the process, the grain orientation and dislocation density are represented by grain growth and the cellular state during the simulation process.
III. The collection of cells distribution in spatial sites is known as cellular space (CS). The CS can be divided into 1D, 2D, 3D, and high-dimensional according to the dimension of space [68,69].
IV. In the 1D-CA model, neighbours are typically determined by radius, and all cells within a cell are considered neighbours of that cell. In the 2D-CA and 3D-CA models, neighbour definition generally takes the von Neumann neighbour type and Moore neighbour type.
V. In the CA model, the state of a cell in the local spatial range at the next moment is determined by the state of itself and the state of its neighbour cells at the current moment. All possible states with the state transformation rules of a cell are responsible for that cell. Different neighbourhood types can transform functions that determine a cell's state at the next step.

CA method has basic features. First, the cell distribution embodies the discreteness of space in the discrete cell space divided according to specific rules (discreteness). The state configuration of each time step (t+1) depends entirely on the previous state configuration of time (t). Its defined transformation function, which reflects the discreteness of time. Second, the change of each cell state in the cell space obeys the same transformation rule (homogeneity). Third, the state of each cell at time t+1 depends on the state of the cells at time t in the neighbourhood (temporal and spatial locality). Forth, each cell is independent in its state at time t+1, without any interaction. This is a synchronous calculation feature or parallelism.

4.3.1. *DRX and DRV equations in CA method*

The DRX and DRV equations in CA method are categorized into dislocation density, nucleation model and growth model.

4.3.1.1. *Dislocation density models*. The evolution of dislocation density models during hot deformation that is commonly used in CA are Kocks-Mecking (KM) and Estrin-Mecking (EM) models (Table 3) [161]. In both KM and EM models, work hardening and dynamic softening effects on the variation of dislocation density are considered.

4.3.1.2. *Nucleation model*. Most of the nucleation models focus on fitting the nucleation rate ($\dot{n}$) of materials in the DRX. Typical DRX nucleation models used at CA are summarized in Table 4. First, in the models presented by Roberts and Ahlblom (RA) and Derby and Ashby (DA), the nucleation rate was related to the strain rate (Sr).

Peck and Luton (PL) developed (RA) and (DA) models by importing the deformation temperature (Dt) in the equation. Ding and Guo (DG) proposed a DRX nucleation model based on Sr, and Dt. Kugler and Turk (KT) proposed a simple model based on probability. In the KT model, once dislocation density (ρ) is higher than critical dislocation density (ρ_{cr}), the probability of recrystallization nucleation of cells is increased. Cram et al. proposed another form of probability-based nucleation model. In their models, the large-angle sub crystal is considered as the potential position of recrystallization. Zou et al. improved the (DG) model by adding the Sr and Dt function with the strain (ε). Jin and Cui (JC), related the dislocation density to the local deformation energy storage inside the material and thus, they established a dislocation-related nucleation model.

4.3.1.3. *DRX growth model*. From a metallurgical point of view, the dislocation density of new recrystallized grains is very low [171–173]. There is a large difference between the dislocation density of new grains and the matrix grains. This situation provides the driving force for the growth of DRX grains. Table 5 lists models for DRX growth that have been widely implemented in the CA modelling [118,174,175].

Minor literature is available about CA simulation of DRX in hot forming for steels [180,181]. Wnag et al. [182] used the CA method for DRX evaluation of FeSiCrNi shape memory alloy under hot compression test. The simulation results show that

Table 4 – Various DRX nucleation models used at CA.

Model Name	Equation	Parameter names	Reference
RA and DA	$\dot{n} = C\dot{\varepsilon}^m$	$\dot{n}$ is basically linear with, m is Material parameter, C is the nucleation parameter.	[162]
PL	$\dot{n}(T) = n(T_m)\dot{\varepsilon}exp\left[-\frac{Q_{act}}{RT_m}\left(\frac{T_m}{T}-1\right)\right]$	n is related to and T, R is the proportional constant, Qact is thermal activation energy.	[163]
DG	$\dot{n}(\dot{\varepsilon},T) = C\dot{\varepsilon}exp\left[-\frac{Q_{act}}{RT}\right]$	n is related to and T, and model's complexity is moderate.	[164–166]
KT	$P = k\dot{\varepsilon}exp(-\frac{\omega}{T})\Delta t$	Probability-based nucleation model, where $\omega = 2100$ K, $k = 8.0$.	[167]
Cram et al.	$P = \frac{64R_i^2}{\pi^2\overline{r}_i^2}exp\left(-\frac{\pi\chi_{c,i}^2}{4}\right)$	Physical mechanism-based nucleation model, where Ri is the grain size.	[168]
Xiao et al.	$\dot{n}(\dot{\varepsilon},Z,\varepsilon) = C\dot{\varepsilon}Z^{m_1}(\varepsilon-\varepsilon_{cr})^{m_2}$	n is related to T, and ε, cr is critical strain, $m1$ and $m2$ are constants, Z is Zener-Hollomon parameter.	[169]
JC	$\dot{n}(\rho) = \frac{\sqrt{\rho}-\sqrt{\rho_{Cr}}}{\sqrt{\rho_s}-\sqrt{\rho_{Cr}}}\dot{n}_s$	Dislocation-related nucleation model, ρ_s is the saturated dislocation density, ρcr is the critical dislocation density, n_s is the n when ρ reached ρ_s.	[170]

the size of recrystallized grains increases with strain rate, but the effect of strain rate is not as significant as temperature. The multilevel cellular automaton framework was used for DRX modelling of 316LN steel by Chen et al. [183]. They used these simulation processes for the monitoring of nucleation and growth of new grains at different strains. In the simulation results, the nucleation and the growth of new grains occur at high energy positions and in unstable states. Wu et al. [184] implemented the CA method to investigate the morphological evolution of DRX and Low-Carbon Microalloyed Steel's microstructures during hot compression. They show that the distribution of DRX is not uniform in all areas of the hot compressed sample. The modelling results revealed that the volume fraction of DRX and recrystallized grain size is different from one position to another, and recrystallized grain size increases with strain. Zhi et al. [185] applied the CA method with physical metallurgy principles to predict TRIP steel DRX phenomena during the hot compression test. They used CA to simulate the size and shape of grains, volume fraction, kinetics curve of DRX. The same procedure has been done by Chen et al. for 30Cr2Ni4MoV rotor steel [178,183]. Microstructure changes during the hot compression test of 11Cr steel (X12 alloy) were investigated with a cellular automaton (CA) model under various deformation conditions by Chen et al. [186]. The simulation results of grain size were compared with the experimental results. The simulation predicted the grain size with an average relative error of 6%. In their simulation, microstructure evolution of 11Cr steel was simulated at 1150 °C and 0.5s^{-1} strain rate for different strain steps whose results are shown in Fig. 10. The initial microstructure size of 11Cr steel was selected near 38.86 μm. As deformation increases, dislocation density gradually increases. When dislocation density oversteps a critical value required for dynamic recrystallization, 11Cr steel begins to enter a dynamic recrystallization process. First, a new grain nucleus begins to form at the grain boundary so that dislocation density at the new nucleation becomes zero. Then a newly formed grain nucleus begins to grow gradually and eventually is stabilized.

Due to available literature, the FEM, CA, MC, and PF methods are widely hired to simulate the recrystallization nucleation and growth phenomena during hot working. Until now, limited researches dealt with the simulation of recrystallization of MSS with MC and CA methods. Also, there is no available data about MSS recrystallization phenomena with PF simulation. In this regard, the cons and pros of these methods about MSS are not very clearly defined. In general, the grain topography discretizes into polygon lattice points in the MC method.

The different morphology of grain structure and various thermo-mechanical phenomena can be used for the micro-mechanical analysis of MSS microstructures by FEM. In microscale FEM, the DRX of investigated metal cannot be modeled, which is a significant issue not considered with this method.

The most significant advantage of the MC method is that simple and easy to implement, and the calculation cost of MC is meager. The results of DRX simulation by MC in the MSS case indicated that the mechanism of grain growth during hot deformation is monitorable. This means that the information on grain size changes and grain morphology evolution can also be visually observed. The first drawback of this method is that arbitrary transformation rules or determinism do not exist in the MC method. The MC method is not scalable, which means the simulation time is not related to the time of physical phenomena. At this point, it is necessary to improve this method to be scalable. In some cases, the MC simulation result's grain growth index is not 100% matched with the theoretical grain growth index. This issue shows that the MC cannot reflect the changes of grain boundaries mechanism during the hot deformation of MSS.

Investigation between different simulation methods for studying DRX during hot deformation of MSS shows that the CA is relatively efficient and flexible. During simulation of DRX phenomena with the CA method, the state of new cells is the consequence of the previous state and neighboring cells. These properties are not in the MC simulation method. This method is scalable, meaning the size of grains and grain growth index results match the actual physical phenomena.

In CA, the curvature, thermodynamic-driven, and energy dissipation mechanisms are introduced in local transformation rules. These mechanisms can make the CA scalable, making the CA method more realistic for the grain boundaries migration results in an actual hot forming process. Like other

Table 5 – DRX growth models in the CA.

Model Name	Equation	Application	Reference
dW—Energy variation value	$dW = dW_{vol} + dW_{sur}$ $\begin{cases} dW_{vol} = 4\pi r_i^2 \tau(\rho_i - \rho_m)dr \\ dW_{sur} = 4\pi r_i \gamma_i dr \end{cases}$	Assume that the newly formed recrystallized grains are spherical. dW_{vol}, dW_{sur} are variations of system volume energy and surface energy, respectively. r_i is the radius of recrystallized grains	[158,163,164]
Fi—Total driving force	$F_i = \frac{dW}{dr} = 4\pi r_i^2 \tau(\rho_m - \rho_i) - 8\pi r_i \gamma_i$	ρ_i is the dislocation density of the i-th grain,	[163,176]
f_i—Driving force of per unit area	$f_i = \frac{F_i}{4\pi r_i^2} = \tau(\rho_m - \rho_i) \frac{2\gamma_i}{r_i}$	ρ_m is the dislocation density of surrounding grains.	[163,176]
γ i—GBE	$\gamma_i = \begin{cases} \gamma_m & \theta_i \geq 15^\circ \\ \gamma_m \frac{\theta_i}{\theta_m}\left(1 - \ln\frac{\theta_i}{\theta_m}\right) & \theta_i \leq 15^\circ \end{cases}$	Read-Shockley equation. θ_i is the misorientation.	[177]
γ m—GBE of LAGB	$\gamma_m = \frac{\mu b \theta_m}{4\pi(1-\nu)}$	θ_m is the misorientation of LAGB (assuming θ_m is 15°). υ is the Poisson ratio.	[178]
Vi—Growth rate	$V_i = Mf_i$	Commonly used DRX grain growth model	[179]
M—Grain boundary mobility	$M = \frac{\delta D_{0b} b}{KT} = exp\left(-\frac{Q_b}{RT}\right)$	δ is the GB thickness, Qb is the GB diffusion activation energy, K is the Boltzmann constant, D_{ob} is the GB self-diffusion coefficient.	[158,163,164]

modeling methods, the CA has disadvantages. In CA, for obtaining the material parameters CA, it is necessary to develop scientific methods and time-consuming and expensive tests. CA model in 2D is much easier than 3D, and the 3D space modeling by CA is required complex algorithms and elements. For this reason, the obtained results from 2D simulations do not always correspond directly to the 3D results.

5. Artificial neural networks application in flow stress prediction of MSS

Artificial Neural Networks (ANNs) constitute a modern computation process designed to simulate physical and chemical processes with how the human brain analyses and processes information [187,188].

The basis of an Artificial Neural Network (ANN) is to emulate the behavior of biological neural systems in digital software using a collection of data or examples. This technique has been extensively used in Information and Communications Technologies (ICTs) in order to solve different issues such as image and handwriting recognition or natural language processing [188,189.

Thus, once the potential for modeling complex tasks has been recognized, and considered the advances during the last years in software/hardware development, Artificial Intelligence (AI) capabilities have been proved in other sectors, like the industrial world and, more precisely, in the manufacturing processes. There are three main reasons for this growth: the AI potential for modeling complex processes in which multiple effects are present without the need for the complete understanding of them, its ability to approximate the nonlinear relationships among the inputs (process parameters) and the outputs (measured parameters), and an outstanding capacity for generalization [190].

Examples of these features of ANNs applied to manufacturing processes can be found in the scientific literature. In a study by Benardos et al. [191,192] an ANN has been used for modeling the surface roughness and its values in face milling, and a comparison between the analytical and the ANN model has been carried out. Concerning the grinding process, Arriandiaga et al. used an alternative to data progress feedforward from the input layer to the output one with Recurrent Neural Networks (RNN) [193]. Finally, regarding Electrical Discharge Machining (EDM), a process typically used for aerospace components, the research works done to reduce its defects can be highlighted [194,195].

The forging process could not be left behind. The complex nonlinear relationship between strain, strain rate, and temperature is a critical point when applying AI in hot deformation.

The first attempts to use ANNs to explain the material's behavior were made with different inputs according to the recently used ones. In the beginning, alloy composition was considered an input parameter, Mandal et al. [196]. However, nowadays, deformation conditions are used to feed the ANN, namely strain, strain rate, and temperature, removing the alloy composition as shown in Fig. 11.

However, several research works have a common point: using the Back Propagation (BP) neural network to estimate the flow stress of several materials. This algorithm is responsible for the learning process of the well-known Multilayer Perceptron (MLP) neural network model, which has served as a basis for more complex models, such as Convolutional Neural Networks needed for image classification. Using this type of ANN is that it is the most suitable tool for treating non-linearities. BP algorithm is a supervised learning method for multilayer feedforward networks. Its principle is to model a function by modifying the internal weights of input signals to produce an output one. Then, the error between this output and a known expected one is used to modify these weights. This supervised learning method can be summed up as follows. In the first round, the network is simulated with the input signal, spreading it through the different layers of the network, producing a result. In a second

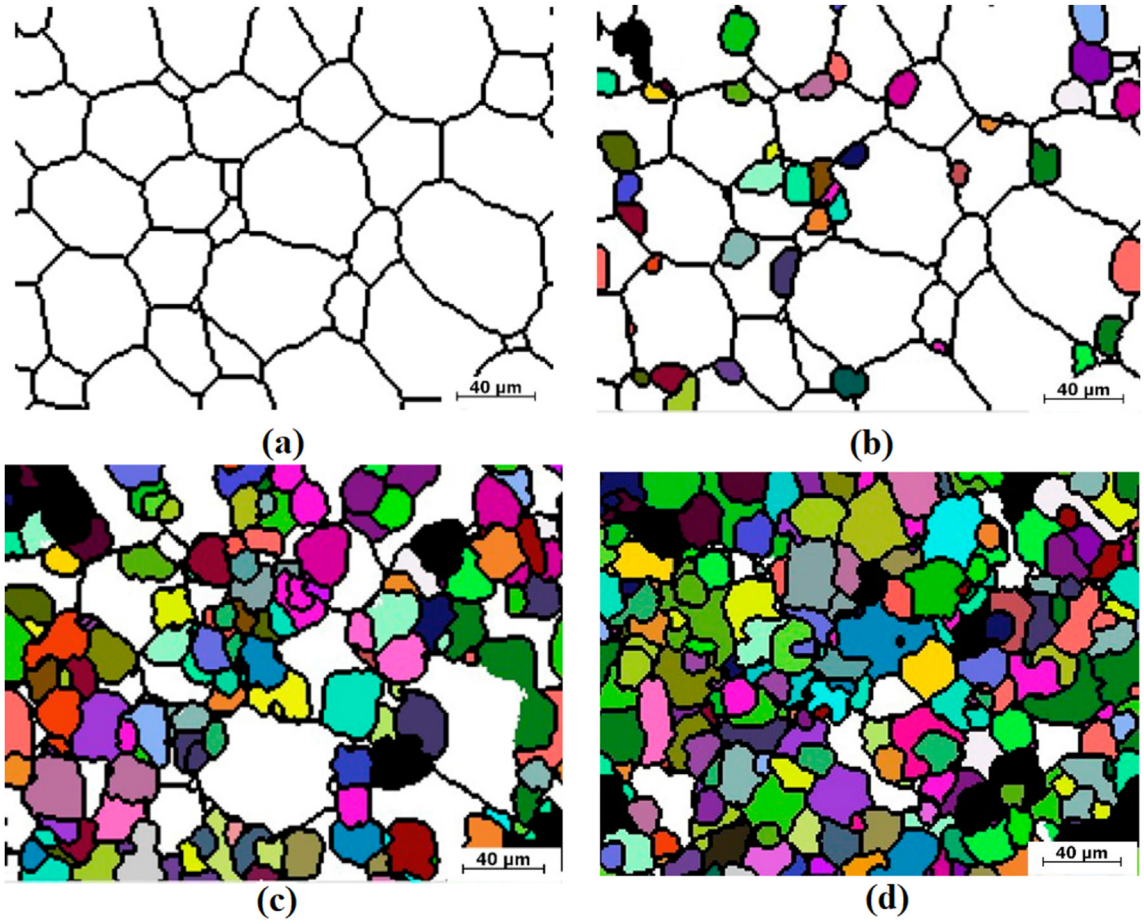

Fig. 10 – CA modelling microstructure evolution of 11Cr steel [186].

round, this result (output) and the target value are compared to obtain an error for each of the outputs. The final aim of this type of ANN is to train it with several data to learn the appropriate internal steps to allow it to learn any arbitrary mapping of pairs of data (inputs and output). Even the general use of this ANN was known thanks to Rumelhart et al. [197] some predecessors can be found. Later, Goodfellow et al. publish an overview of this type of learning method A standard or basic network structure consists of one input layer, one hidden layer, and one output layer. The structure can be defined as one fully connected layer to the next one if required, as depicted in Fig. 12. Hence, based on the input variables strain, strain rate, and temperature, this work [12] attempts to develop a backpropagation neural network model to predict the flow stress as output.

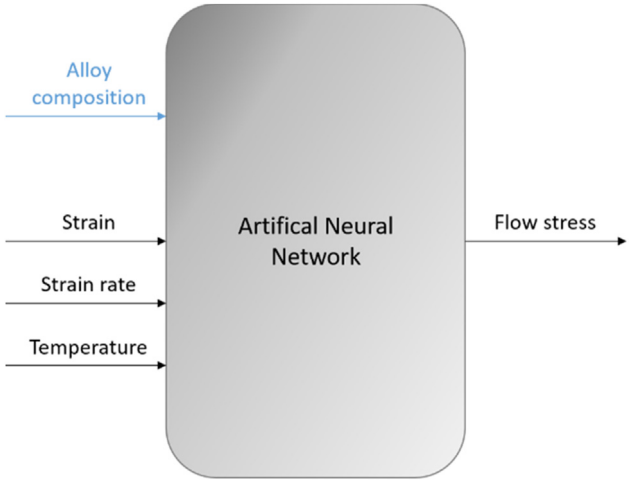

Fig. 11 – Schematic configuration of the ANN structure model.

Hence, Mandal et al. [195,196] used this structure in austenitic stainless steels behavior with 1 layer and 15 neurons in the hidden one as the optimum configuration. This ANN was checked with different statistical parameters, such as correlation coefficient, scatter index, and average absolute relative error that describe in Eqs. (95)–(97).

$$R = \frac{\sum_{i=1}^{n}(T_i - \overline{T})(A_i - \overline{A})}{\sqrt{\sum_{i=1}^{n}(T_i - \overline{T})^2 \sum_{i=1}^{n}(A_i - \overline{A})^2}} \tag{95}$$

$$SI = \frac{RMSE}{\overline{T}} \tag{96}$$

$$AARE = \frac{1}{n}\sum_{i=1}^{n}\left|\frac{T_i - A_i}{T_i}\right| 100 \tag{97}$$

where T and A represent the flow stress values in MPa of the experimental data and approximated dataset, respectively. n is the number of elements in the flow stress vector.

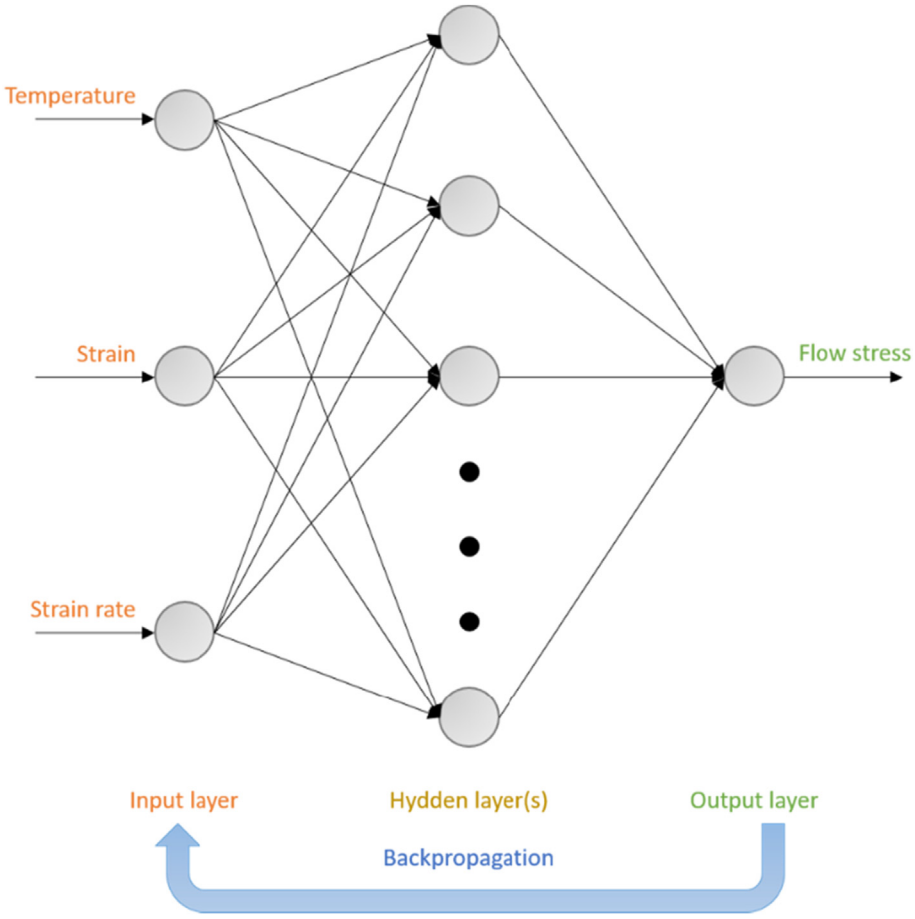

Fig. 12 – Schematic diagram of the Back-Propagation (BP) ANN structure representing inputs and outputs of the model.

These equations are often used to check the ANN accuracy and validate it. The first one is the Pearson's correlation coefficient adjustment to a sample, which can be defined as the ratio between the covariance of two variables and the product of their standard deviations. In other words, it provides the strength of the linear relationship between the experimental data and the ANN outputs.

The scatter index is obtained by the relation between the average root mean square error (RMSE) (Equation (98)) and the mean values of experimental findings.

$$RMSE = \frac{1}{n}\sum_{i=1}^{n}\left[\sum_{j=1}^{p}\left(A_{ij} - T_{ij}\right)^2\right]^{1/2} \quad (98)$$

Hence, the RMSE represents the square root of the second moment of the sample of the differences between the predicted values and the observed values or the root mean square of these differences, and it is used to aggregate the magnitudes of the errors in the predictions for several times in a single measure of predictive power.

Finally, the average absolute relative error (AARE) quantifies the ANN's effectiveness in its ability to accurately predict data from a calibrated model [198].

Then, in a later paper works, they focused more deeply on the prediction of deformation behavior under warm and hot torsion of 304L stainless steel as a function of process variables and the prediction of microstructural evolution as a function of process parameters during thermo-mechanical processing of alloy D9 [199,200]. In order to do so, they used the same ANN structure, varying the number of neurons implemented.

A BP artificial neural network has been trained and employed in the flow stress simulation of 316 austenitic stainless steel, particularly in a dynamic strain-aging regime [201]. Compared to the experimental tests, the results showed that the maximum error between predicted and experimental data is less than 8.67%, and the correlation coefficient (R) is 0.9955, concluding that predicted flow stress by the artificial neural network is in good agreement with experimental results.

Singh et al. [202] study the behavior of hot compression of high phosphorus steel. Experiments were carried out in a range of temperatures of 750 °C - 1050 °C and strain rates between 0.001 s^{-1} and $10s^{-1}$. The experimental stress–strain data were introduced in an ANN to check the predictability of the flow stress. The structure trained is a multilayer model based on a feedforward backpropagation algorithm (BP), consisting of three input layers and one hidden layer. The performance of this net has been measured with a relative error of ±3.5% (predicted VS experimental stress) and a correlation coefficient (R^2) of 0.99986 (during the training) and 0.99999 (in the testing process). The authors concluded that a well-trained model has excellent capability to predict the hot deformation behavior of materials.

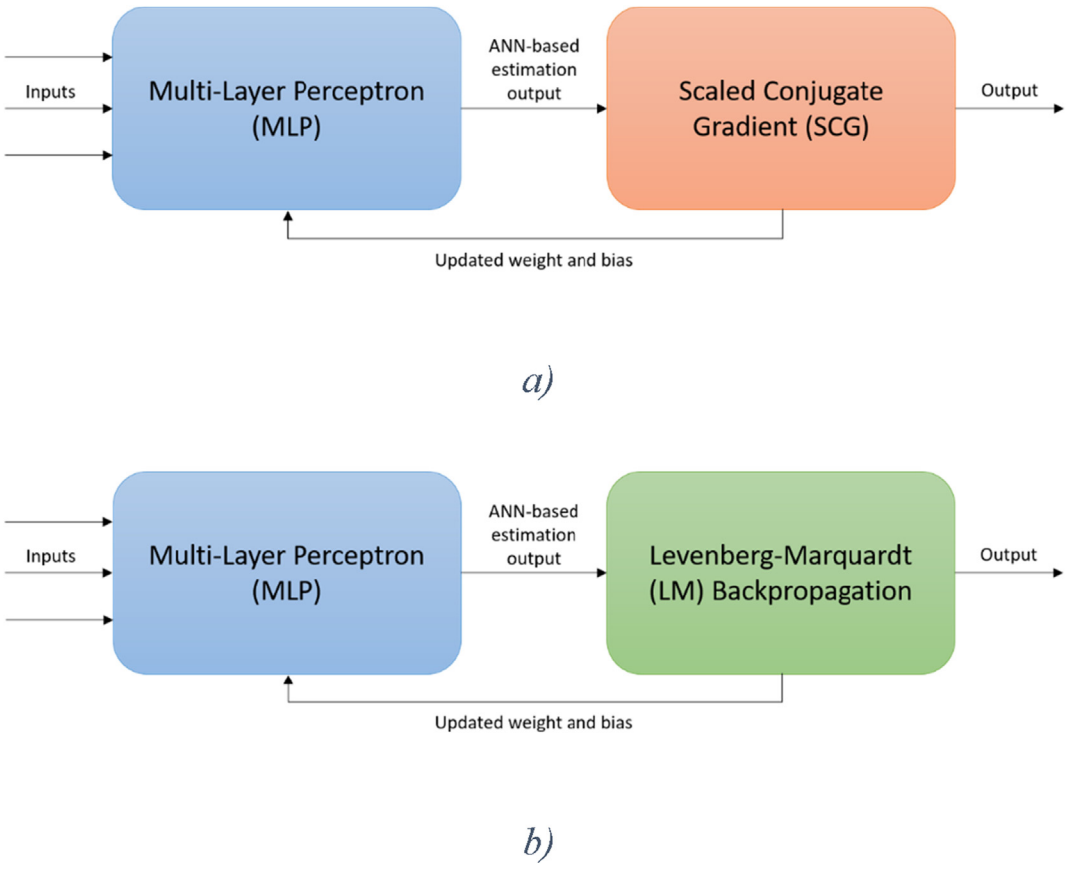

Fig. 13 – Schematic diagram of the Multi-Layer Perceptron (MLP) with a) Scaled Conjugate Gradient (SCG) model; b) Levenberg-Marquardt Backpropagation (LM) model.

Regarding martensitic stainless steels, several research works can be found in which they compare the theoretical or experimental material behavior with an artificial neural network-based model, with the same structure shown in Fig. 11. Hence, Han et al. [203] for instance, focused on the super 13Cr MSS behavior, selecting a BP ANN with sigmoid activation function, with one hidden layer, three neurons, and ten hidden neurons. The mentioned research predicts flow stress by considering temperature, strain, and strain rate as input variables. The tests carried out were accomplished in a range of 950°C–1200 °C temperature and 0.1–50s^{-1} strain rate range, randomly divided into 252 to develop the ANN and 84 to test it. The network's performance has been measured with the root mean square error (RMSE) value.

As a result, the relative error in the prediction is between −7.34% and 2.43%, indicating that the ANN predictions are in line with the experimental data. The first attempts to describe material deformation basic information and finite element simulation can be highlighted from this research work and model.

Shokry et al. [204] tried to establish a model that provides the hot deformation behavior of the flow stresses of the X12 (10% Cr steel) alloy, using the modified Johnson–Cook and strain-compensated Arrhenius-type (phenomenological models) and two enhanced ANNs. The data was introduced in a Multilayer Perceptron (MLP) network in addition to, on the one hand, Scaled Conjugate Gradient (SCG) structure and, on the other hand, in a Levenberg-Marquardt (LM) Back-propagation (shown in Fig. 13).

Backpropagation is used to calculate performance derivatives concerning the weight and bias; the scaled conjugate gradient (SCG) algorithm is based on conjugate directions, without performing a line search at each iteration in other conjugate gradient algorithms. More detailed information could be found in Moller's research paper. On the other hand, the Levenberg – Marquardt algorithm [205] is specifically used to solve nonlinear least-squares problems, so it is designed to minimize sum-of-squares error functions, finding its minimum value, even if it is the local, instead of the global one. Nevertheless, this algorithm is more robust than other ones, which means that it finds a solution in many cases even if it starts far away from the final minimum.

The performance of the established models was evaluated using these four statistical parameters: correlation coefficient (R), Average Absolute Relative Error (AARE), Root Mean Squared Error (RMSE), and Relative Error (RE).

The ANN-based models showed higher prediction accuracy, with best results (R = 0.99992, AARE = 0.748% and RMSE = 0.441 MPa) for the LM AN. Besides, the authors highlighted the non-linearity of the parameters (strain, strain rate,

and temperature). This statement justifies the better results for the ANN since the flow behavior became highly nonlinear and complex at some temperature ranges.

Krishna et al. [97]follow the same structure in search of the nitrogen alloyed martensitic stainless steel behavior (Fe-15.9Cr-1.7Mo-0.43C-0.14Nb-0.22N (wt%). They used the BP algorithm with different configurations (activation functions, number of neurons in hidden layer …) to look for the one that best fits the material's behavior. The final selection uses three layers (input, hidden, and output layer) with 17 neurons in the hidden layer. The model showed an average absolute relative error (AARE) of 19.6% and a correlation coefficient (R) of 0.975. The authors concluded that Johnson–Cook (JC) model showed an average absolute relative error (AARE) and correlation coefficient (R) worse than the modified-JC model that reached an accuracy of 1.2% (AARE) and 0.994 (R). However, the ANN predicted the output better than the previous models with an AARE of 0.3%.

An example of making processing maps of the material for Cr–Mo low-alloyed steel can be found in the work of Opela et al. [206], where they used an MLP neural network with two hidden layers, each with eight hidden neurons that were activated via hyperbolic-tangent sigmoid function. This ANN was trained with five temperatures (805, 885, 980, 1085, and 1210 °C) under the experimentally tested strain rate levels. The performance of this MLP was evaluated with the Pearson's correlation coefficient, R (–), and the average absolute relative error, AARE (%). The statistical indicators exhibit a good fit with a value of R = 0.999904 and AARE = 1.0298, respectively.

In conclusion, experimental data (uniaxial hot compression tests with 1.0 true strain in the temperature range of 770–1280 °C and the strain rate range of 0.02–20s^{-1}) and MLP network were combined to assemble processing maps with five additional temperature levels obtained from the software it can be highlighted.

The behavior of 9Cr–1Mo steel has been analyzed by Kumar et al. [207]. The constitutive model covered a range of 850°C–1100 °C in temperature and 0.001s^{1}–10s^{-1} in strain rate. The corrections of flow stress have been made by comparing the artificial neural network (ANN) and the linear interpolation method with the predicted flow stress obtained by a constitutive equation. In order to do so, the structure of the network has been set with one input layer, one hidden layer with 21 neurons in each one, and one output layer. The model's accuracy has been checked with the correlation coefficient, mean absolute error (MAE), and relative error (RE).

$$MAE = \frac{1}{n}\sum_{i=1}^{n}\left|\frac{E_i - P_i}{E_i}\right| \tag{99}$$

$$RE = \frac{E_i - P_i}{E_i}100\% \tag{100}$$

where n is the number of training/testing data, E_i is the experimental value, and P_i is the predicted one. As a result, it can be highlighted that processing maps corrected through ANN showed the best precise results over that of the conventional method.

The revised articles showed the utility of ANNs (MLP network in several cases) and how it can be improved by testing different techniques and optimization tools, such as SCG or LM-BP. The use of these techniques is justified due to the complex nonlinear relationship among strain, strain rate, and temperature, which is a critical point in hot deformation and one of the powerful advantages of the ANNs. Their application is increasing rapidly in the manufacturing sector as a different approach for solving this complex problem. However, the critical point of the use and improvement of these techniques is the capability of data acquisition. Once, these acquisition methods and the amount of data storage improve, it would result in a rise in the effectiveness of the AI. Nevertheless, the effort needed in order to train, test and use the ANN, even if improves the precision of material behavior, is greater in comparison with the results obtained nowadays.

6. Conclusions and future work

This article reviews the studies in the simulation of Dynamic recrystallization and grain evolution of MSS during hot forming. It can be discovered that in recent years, the physical base modeling in the macroscale modeling section and the CA method in the microscale section has been becoming powerful tool for quantitative and explicit simulation of microstructure evolution of MSS during the hot manufacturing process. On the other hand, the implementation of ANN for this class of steel is in the early stage. Due to available literature, it can be seen that many interesting outputs have been achieved, especially in the field of macroscale modeling. Nevertheless, some aspects still deserve further investigation:

(1) It is essential to find developed or new Mathematical parameters in dynamic recrystallization of MSS that do not consider their behavior during Hot forming process. With increasing industrial needs, scientists improved or made new steels classified as MSS, and some have not been put in hot deformation conditions. In this case, developing mathematical models to understand these MSS steel could be helpful to industries and researchers.
(2) It is essential to develop models of DRX in MSS on a microscale to understand metallurgical changes during hot deformation better. As discussed, the general point of view of DRX modeling in microscale is related to the hot compression and hot tension test. However, in the actual situation, there are a couple of manufacturing processes containing several steps from billet to final product, that all are in hot condition. In this issue, finding a developed method for simulation of DRX during multistep hot deformation process (with various types of stresses) is seems necessary.
(3) Until now, no results have reported a model considered recrystallization nucleation parameters in MC or CA models in MSS steels. Usually, nucleation parameters are considered by metallographic tests or inverse analysis optimization algorithms, and after that, the results are imported to the MC or CA methods as a matrix to solve the equations. Metallographic tests are unreliable due to human errors, and it is also challenging to

distinguish the matrix grains and recrystallized grains in the same field. The inverse analysis optimization algorithm problem is that it is not possible to implement in 3D CA.

(4) The microscale models in 2D and 3D need fewer complex algorithms and elements to make CA or MC fast and straightforward. The simple algorithms for solving a series of problems caused by complex plastic deformation, high strain rate, and severe plastic deformation in microscale decrease solving time, increased accuracy for multi-scale simulation, and improved computational efficiency.

(5) The ANN field in the simulation of MSS behavior in macro and microscale is in the early stage. Many issues can be considered by ANN, especially on a microscale. For this reason, it can be concluded that all previous methods that considered finding new information that cannot be considered by macro or microscale may reveal with ANN in the future.

Author contributions

Hamed Aghajani Derazkola: Conceptualization, Investigation, Writing- original draft. **Eduardo Garcia:** Supervision, Project administration, Writing-review & editing. **Alberto Murillo-Marrodán:** Conceptualization, Investigation, Writing- original draft. **Aintzane Conde Fernandez:** Conceptualization, Investigation, Writing- original draft.

Declaration of Competing Interest

The authors declare that they have no known competing financial interests or personal relationships that could have appeared to influence the work reported in this paper.

Acknowledgment

This project has received funding from the European Union's Horizon 2020 Research and Innovation Programme under the Marie Skłodowska-Curie grant agreement No. 847624. In addition, a number of institutions back and co-finance this project.The paper reflects only the authors' view and the Agency is not responsible for any use that may be made of the information it contains.

REFERENCES

[1] Stichel W. ASM speciality handbook: stainless steels. 577 S. In: von J Hrsg, Davis R, editors. Europa zu beziehen durch: American Technical Publishers Ltd, 27–29 Knowl Pi. Mater. Corros. vol. 46. Materials Park, Ohio, USA: ASM International; 1994–95. p. 499. https://doi.org/10.1002/maco.19950460815. £ 136.00 (ASM Member £ 102.00) ISBN 0-87170-503-6.

[2] Webster D. Development of a high strength stainless steel with improved toughness and ductility. Metall Mater Trans B 1971;2:2097–104. https://doi.org/10.1007/BF02917537.

[3] Hara T, Semba H, Amaya, H.B.T.-R.M. in M.S. and M.E.. In: Caballero,F.G.B.T.-E. of M.M. and A, editor. Pipe and tube steels for oil and gas industry and thermal power plant. Oxford: Elsevier; 2020. p. 140–52. ISBN 978-0-12-819733-2.

[4] Garrison WM, Amuda, M.O.H.B.T.-R.M. in M.S. and M.E.. Stainless steels: martensitic. Elsevier; 2017. ISBN 978-0-12-803581-8.

[5] Manilova E. Examination of minor phases in martensitic 12% Cr-Mo-W-V steel. Microsc Microanal 2006;12:1612–3. https://doi.org/10.1017/S1431927606064786.

[6] Villalobos JC, Del-Pozo A, Campillo B, Mayen J, Serna S. Microalloyed steels through history until 2018: review of chemical composition, processing and hydrogen service. Met 2018;8.

[7] Zhu H, Chen F, Zhang H, Cui Z. Review on modeling and simulation of microstructure evolution during dynamic recrystallization using cellular automaton method. Sci China Technol Sci 2020;63:357–96. https://doi.org/10.1007/s11431-019-9548-x.

[8] Hemmati I, Ocelík V, De Hosson JTM. Microstructural characterization of AISI 431 martensitic stainless steel laser-deposited coatings. J Mater Sci 2011;46:3405–14. https://doi.org/10.1007/s10853-010-5229-2.

[9] Derazkola HA, García Gil E, Murillo-Marrodán A, Méresse D. Review on dynamic recrystallization of martensitic stainless steels during hot deformation: Part I—experimental study. Met 2021:11.

[10] Zhang H, Wei Z, Xie F, Sun B. Assessment of the properties of AISI 410 martensitic stainless steel by an eddy current method. Mater 2019;12.

[11] Lenda O Ben, Tara A, Lazar F, Jbara O, Hadjadj A, Saad E. Structural and mechanical characteristics of AISI 420 stainless steel after annealing. Strength Mater 2020;52:71–80. https://doi.org/10.1007/s11223-020-00151-4.

[12] Giordana MF, Alvarez-Armas I, Armas A. On the cyclic softening mechanisms of reduced activity ferritic/martensitic steels. Steel Res Int 2012;83:594–9. https://doi.org/10.1002/srin.201100254.

[13] Garrison WM. Stainless steels: martensitic. In: Buschow KHJ, Cahn RW, Flemings MC, Ilschner B, Kramer EJ, Mahajan S, editors. Veyssière, P.B.T.-E. of M.S. and T. Oxford: Elsevier; 2001. p. 8804–10. ISBN 978-0-08-043152-9.

[14] Zhang J, Li J, Shi C, Huang J. Growth and agglomeration behaviors of eutectic M7C3 carbide in electroslag remelted martensitic stainless steel. J Mater Res Technol 2021;11:1490–505. https://doi.org/10.1016/j.jmrt.2021.01.113.

[15] Dourandish S, Jahazi M, Ebrahimi GR, Ebacher L. Influence of eutectic phase precipitation on cracking susceptibility during forging of a martensitic stainless steel for turbine shaft applications. J Mater Res Technol 2021;13:260–70. https://doi.org/10.1016/j.jmrt.2021.04.075.

[16] Ning J, Zhang H-B, Chen S-M, Zhang L-J, Na SJ. Intensive laser repair through additive manufacturing of high-strength martensitic stainless steel powders (II): evaluation of intensive repair ability of high strength martensitic steel powder based on Schaeffler diagram. J Mater Res Technol 2022;16:1494–507. https://doi.org/10.1016/j.jmrt.2021.12.015.

[17] El-Aziz KA, Saber D. Mechanical and microstructure characteristics of heat-treated of high-Cr WI and AISI4140 steel bimetal beams. J Mater Res Technol 2020;9:7926–36. https://doi.org/10.1016/j.jmrt.2020.05.017.

[18] Li W, Qin S, Li Y, Wang Y, Jiang P, Tong W. Friction resistance and bonding strength of high vanadium alloy steel/low carbon steel bimetal after heat treatments. J Mater

Res Technol 2021;11:1678–87. https://doi.org/10.1016/j.jmrt.2021.02.007.
[19] Liang Y, Yan W, Shi X, Li Y, Wang W, Shi Q, et al. Transfer from M3B2 boride to BN nitride in 9Cr3W3CoB martensitic heat-resistant steel. J Mater Res Technol 2021;13:513–23. https://doi.org/10.1016/j.jmrt.2021.05.004.
[20] Yang Q, Zhou Y, Li Z, Mao D. Effect of hot deformation process parameters on microstructure and corrosion behavior of 35CrMoV steel. Mater 2019;12.
[21] Singh R. In: Singh, R.B.T.-A.W.E., editor. Chapter 6 - Welding corrosion resistant alloys – stainless steel. Boston: Butterworth-Heinemann; 2012. p. 191–214. ISBN 978-0-12-391916-8.
[22] Magnee A, Drapier JM, Coutsouradis D, Habrakan L, Dumont J. Cobalt-containing high-strength steels. 1974. Belgium.
[23] Raabe D. In: Laughlin DE, Hono, K.B.T.-P.M., editors. 23 - Recovery and recrystallization: phenomena, physics, models, simulation. 5th ed. Oxford: Elsevier; 2014. p. 2291–397. ISBN 978-0-444-53770-6.
[24] Pickering FB. Physical metallurgy and the design of steels/F. B. Pickering; Materials science series (London, England). London: Applied Science Publishers; 1978. ISBN 0853347522.
[25] Rafi HK, Starr TL, Stucker BE. A comparison of the tensile, fatigue, and fracture behavior of Ti–6Al–4V and 15-5 PH stainless steel parts made by selective laser melting. Int J Adv Manuf Technol 2013;69:1299–309. https://doi.org/10.1007/s00170-013-5106-7.
[26] Sakai T, Belyakov A, Kaibyshev R, Miura H, Jonas JJ. Dynamic and post-dynamic recrystallization under hot, cold and severe plastic deformation conditions. Prog Mater Sci 2014;60:130–207. https://doi.org/10.1016/j.pmatsci.2013.09.002.
[27] Rollett AD. Overview of modeling and simulation of recrystallization. Prog Mater Sci 1997;42:79–99. https://doi.org/10.1016/S0079-6425(97)00008-X.
[28] Rusty, Gray GT. High-strain-rate deformation: mechanical behavior and deformation substructures induced. Annu Rev Mater Res 2012;42:285–303. https://doi.org/10.1146/annurev-matsci-070511-155034.
[29] Chen X, Li Q, Pan J, Liu J, Wei X, Chen S. Experimental study on stress corrosion of X12Cr13 stainless steel in natural gas environment. J Mater Res Technol 2020;9:3064–74. https://doi.org/10.1016/j.jmrt.2020.01.037.
[30] Hou Z, Chen S, Sun Q, Wei X, Lv W. Experimental research on fatigue characteristics of X12Cr13 stainless steel. J Mater Res Technol 2020;9:3230–40. https://doi.org/10.1016/j.jmrt.2020.01.070.
[31] Wang Y, Hu Y, Mao F, Li J, Zhou J, Zhang S, et al. Microstructure evolution and mechanical properties of bimodal grain sized 301 stainless steel strip induced by reverse phase transformation. J Mater Res Technol 2022;17:2772–81. https://doi.org/10.1016/j.jmrt.2022.01.168.
[32] Humphreys FJ, Hatherly M. In: Humphreys FJ, Hatherly, M.B.T.-R. and R.A.P., editors. Chapter 8 - Recrystallization of ordered materials. 2nd ed. Oxford: Elsevier; 2004. p. 269–83. ISBN 978-0-08-044164-1.
[33] Yang Y, Yan Q, Ge C. Hot deformation behavior of modified CNS- II F/M steel. J Iron Steel Res Int 2012;19:60–5. https://doi.org/10.1016/S1006-706X(12)60048-X.
[34] Zhang Y, Hu M, Cai Z, Han C, Li X, Huo X, et al. Effect of nickel-based filler metal types on creep properties of dissimilar metal welds between Inconel 617B and 10% Cr martensitic steel. J Mater Res Technol 2021;14:2289–301. https://doi.org/10.1016/j.jmrt.2021.07.131.
[35] Mao W, Gao S, Bai Y, Park M, Shibata A, Tsuji N. Effective grain size refinement of an Fe-24Ni-0.3C metastable austenitic steel by a modified two-step cold rolling and annealing process utilizing the deformation-induced martensitic transformation and its reverse transformation. J Mater Res Technol 2022;17:2690–700. https://doi.org/10.1016/j.jmrt.2022.02.031.
[36] McQueen HJ, Jonas JJ. Recovery and recrystallization during high temperature deformation. In: ARSENAULT, R.J.B.T.-T. on M.S.& T., editor. Plastic deformation of materials, vol. 6. Elsevier; 1975. p. 393–493. ISBN 0161-9160.
[37] Sugimoto K. Recent progress of low and medium-carbon advanced martensitic steels. Met 2021:11.
[38] Humphreys FJ, Hatherly M. In: Humphreys FJ, Hatherly, M.B.T.-R. and R.A.P., editors. Chapter 5 - the mobility and migration of boundaries. 2nd ed. Oxford: Elsevier; 2004. p. 121–67. ISBN 978-0-08-044164-1.
[39] Tasan CC, Diehl M, Yan D, Bechtold M, Roters F, Schemmann L, et al. An overview of dual-phase steels: advances in microstructure-oriented processing and micromechanically guided design. Annu Rev Mater Res 2015;45:391–431. https://doi.org/10.1146/annurev-matsci-070214-021103.
[40] Kassner ME, Barrabes SR. New developments in geometric dynamic recrystallization. Mater Sci Eng, A 2005;410–411:152–5. https://doi.org/10.1016/j.msea.2005.08.052.
[41] Li C, Liu Y, Tan Y, Zhao F. Hot deformation behavior and constitutive modeling of H13-mod steel. Met 2018;8.
[42] Xu Y, Liu JS, Jiao YX. Hot deformation behavior and dynamic recrystallization characteristics of 12Cr ultra-super-critical rotor steel. Met Mater Int 2019;25:823–37. https://doi.org/10.1007/s12540-019-00253-y.
[43] Fang Y, Chen X, Madigan B, Cao H, Konovalov S. Effects of strain rate on the hot deformation behavior and dynamic recrystallization in China low activation martensitic steel. Fusion Eng Des 2016;103:21–30. https://doi.org/10.1016/j.fusengdes.2015.11.036.
[44] Ahmadabadi RM, Naderi M, Mohandesi JA, Cabrera JM. Dynamic recrystallization behavior of AISI 422 stainless steel during hot deformation processes. J Mater Eng Perform 2018;27:560–71. https://doi.org/10.1007/s11665-018-3153-9.
[45] Prasad YVRK, Seshacharyulu T. Modelling of hot deformation for microstructural control. Int Mater Rev 1998;43:243–58. https://doi.org/10.1179/imr.1998.43.6.243.
[46] Dehghan-Manshadi A, Barnett MR, Hodgson PD. Recrystallization in AISI 304 austenitic stainless steel during and after hot deformation. Mater Sci Eng, A 2008;485:664–72. https://doi.org/10.1016/j.msea.2007.08.026.
[47] Mehtonen SV, Karjalainen LP, Porter DA. Hot deformation behavior and microstructure evolution of a stabilized high-Cr ferritic stainless steel. Mater Sci Eng, A 2013;571:1–12. https://doi.org/10.1016/j.msea.2013.01.077.
[48] Ragab M, Liu H, Yang G-J, Ahmed MMZ. Friction stir welding of 1Cr11Ni2W2MoV martensitic stainless steel: numerical simulation based on coupled eulerian Lagrangian approach supported with experimental work. Appl Sci 2021:11.
[49] Gao F, Liu Z, Misra RDK, Liu H, Yu F. Constitutive modeling and dynamic softening mechanism during hot deformation of an ultra-pure 17%Cr ferritic stainless steel stabilized with Nb. Met Mater Int 2014;20:939–51. https://doi.org/10.1007/s12540-014-5020-z.
[50] Cai X, Hu X-Q, Zheng L-G, Li D-Z. Hot deformation behavior and processing maps of 0.3C–15Cr–1Mo–0.5N high nitrogen martensitic stainless steel. Acta Metall. Sin. (English Lett. 2020;33:693–704. https://doi.org/10.1007/s40195-019-00991-3.
[51] Momeni A, Dehghani K. Characterization of hot deformation behavior of 410 martensitic stainless steel using constitutive equations and processing maps. Mater Sci Eng, A 2010;527:5467–73. https://doi.org/10.1016/j.msea.2010.05.079.

[52] Momeni A, Dehghani K, Heidari M, Vaseghi M. Modeling the flow curve of AISI 410 martensitic stainless steel. J Mater Eng Perform 2012;21:2238–43. https://doi.org/10.1007/s11665-012-0172-9.
[53] Kevanlo E, Ebrahimi GR, Sani SAA, Momeni A. Dynamic recrystallization kinetics of AISI 403 stainless steel using hot compression test. Iran. J. Mater. Form. 2014;1:32–43. https://doi.org/10.22099/ijmf.2014.2488.
[54] Momeni A, Dehghani K, Keshmiri H, Ebrahimi GR. Hot deformation behavior and microstructural evolution of a superaustenitic stainless steel. Mater Sci Eng, A 2010;527:1605–11. https://doi.org/10.1016/j.msea.2009.10.051.
[55] Momeni A, Dehghani K. Prediction of dynamic recrystallization kinetics and grain size for 410 martensitic stainless steel during hot deformation. Met Mater Int 2010;16:843–9. https://doi.org/10.1007/s12540-010-1024-5.
[56] Sellars CM, Tegart WJM. Hot workability. Int Metall Rev 1972;17:1–24. https://doi.org/10.1179/imtlr.1972.17.1.1.
[57] Momeni A, Dehghani K, Ebrahimi GR, Keshmiri H. Modeling the flow curve characteristics of 410 martensitic stainless steel under hot working condition. Metall Mater Trans A 2010;41:2898–904. https://doi.org/10.1007/s11661-010-0350-z.
[58] Ren F, Chen F, Chen J. Investigation on dynamic recrystallization behavior of martensitic stainless steel. Adv Mater Sci Eng 2014;2014:986928. https://doi.org/10.1155/2014/986928.
[59] Ebrahimi GR, Keshmiri H, Mazinani M, Maldar A, Haghshenas M. Multi-stage thermomechanical behavior of AISI 410 martensitic steel. Mater Sci Eng, A 2013;559:520–7. https://doi.org/10.1016/j.msea.2012.08.136.
[60] Poliak EI, Jonas JJ. Initiation of dynamic recrystallization in constant strain rate hot deformation. ISIJ Int 2003;43:684–91. https://doi.org/10.2355/isijinternational.43.684.
[61] Najafizadeh A, Jonas JJ. Predicting the critical stress for initiation of dynamic recrystallization. ISIJ Int 2006;46:1679–84. https://doi.org/10.2355/isijinternational.46.1679.
[62] Mirzadeh H, Najafizadeh A. The rate of dynamic recrystallization in 17-4 PH stainless steel. Mater Des 2010;31:4577–83. https://doi.org/10.1016/j.matdes.2010.05.052.
[63] Sellars CM, McTegart WJ. On the mechanism of hot deformation. Acta Metall 1966;14:1136–8. https://doi.org/10.1016/0001-6160(66)90207-0.
[64] Zener C, Hollomon JH. Effect of strain rate upon plastic flow of steel. J Appl Phys 1944;15:22–32. https://doi.org/10.1063/1.1707363.
[65] Huang D, Feng W. Hot deformation characteristics and processing map of FV520B martensitic precipitation-hardened stainless steel. J Mater Eng Perform 2019;28:2281–91. https://doi.org/10.1007/s11665-019-03974-8.
[66] McQueen HJ, Ryan ND. Constitutive analysis in hot working. Mater Sci Eng, A 2002;322:43–63. https://doi.org/10.1016/S0921-5093(01)01117-0.
[67] Mirzadeh H, Cabrera JM, Prado JM, Najafizadeh A. Hot deformation behavior of a medium carbon microalloyed steel. Mater Sci Eng, A 2011;528:3876–82. https://doi.org/10.1016/j.msea.2011.01.098.
[68] Ning Y, Yao Z, Guo H, Fu MW. Hot deformation behavior and hot working characteristic of Nickel-base electron beam weldments. J Alloys Compd 2014;584:494–502. https://doi.org/10.1016/j.jallcom.2013.09.112.
[69] de Oliveira TS, Silva ES, Rodrigues SF, Nascimento CCF, Leal VS, Reis GS. Softening mechanisms of the AISI 410 martensitic stainless steel under hot torsion simulation. Mater Res 2017;20:395–406. https://doi.org/10.1590/1980-5373-mr-2016-0795.
[70] Akhmed'yanov AM, Rushchits SV, Smirnov MA. Hot deformation of martensitic and supermartensitic stainless steels. Mater Sci Forum 2016;870:259–64. https://doi.org/10.4028/www.scientific.net/MSF.870.259.
[71] Anoop CR, Prakash A, Giri SK, Narayana Murty SVS, Samajdar I. Optimization of hot workability and microstructure control in a 12Cr-10Ni precipitation hardenable stainless steel: an approach using processing maps. Mater Char 2018;141:97–107. https://doi.org/10.1016/j.matchar.2018.04.025.
[72] Cao Y, Di H, Misra RDK, Yi X, Zhang J, Ma T. On the hot deformation behavior of AISI 420 stainless steel based on constitutive analysis and CSL model. Mater Sci Eng, A 2014;593:111–9. https://doi.org/10.1016/j.msea.2013.11.030.
[73] Chegini M, Aboutalebi MR, Seyedein SH, Ebrahimi GR, Jahazi M. Study on hot deformation behavior of AISI 414 martensitic stainless steel using 3D processing map. J Manuf Process 2020;56:916–27. https://doi.org/10.1016/j.jmapro.2020.05.008.
[74] Feng H, Jiang Z-H, Li H-B, Jiao W-C, Li X-X, Zhu H-C, et al. Hot deformation behavior and microstructural evolution of high nitrogen martensitic stainless steel 30Cr15Mo1N. Steel Res Int 2017;88:1700149. https://doi.org/10.1002/srin.201700149.
[75] Han X, Zhao S, Zhang C, Fan S, Xu F. Prediction of FV520B steel flow stresses at high temperature and strain rates. High Temp Mater Process 2015;34:529–38. https://doi.org/10.1515/htmp-2014-0019.
[76] Kishor B, Chaudhari GP, Nath SK. Hot deformation characteristics of 13Cr-4Ni stainless steel using constitutive equation and processing map. J Mater Eng Perform 2016;25:2651–60. https://doi.org/10.1007/s11665-016-2159-4.
[77] Li X, Hou L, Wei Y, Wei Z. Constitutive equation and hot processing map of a nitrogen-bearing martensitic stainless steel. Met 2020:10.
[78] Mirzadeh H, Najafizadeh A. Hot deformation and dynamic recrystallization of 17-4 PH stainless steel. ISIJ Int 2013;53:680–9. https://doi.org/10.2355/isijinternational.53.680.
[79] Ren F, Chen J, Chen F. Constitutive modeling of hot deformation behavior of X20Cr13 martensitic stainless steel with strain effect. Trans Nonferrous Metals Soc China 2014;24:1407–13. https://doi.org/10.1016/S1003-6326(14)63206-4.
[80] Ren F, Chen F, Chen J, Tang X. Hot deformation behavior and processing maps of AISI 420 martensitic stainless steel. J Manuf Process 2018;31:640–9. https://doi.org/10.1016/j.jmapro.2017.12.015.
[81] Qi R-S, Jin M, Guo B-F, Liu X-G, Chen L. Hot-deformation behavior and hot-processing maps of AISI 410 martensitic stainless steel. High Temp Mater Process 2016;35:929–40. https://doi.org/10.1515/htmp-2015-0145.
[82] Xiao Y-H, Guo C. Constitutive modelling for high temperature behavior of 1Cr12Ni3Mo2VNbN martensitic steel. Mater Sci Eng, A 2011;528:5081–7. https://doi.org/10.1016/j.msea.2011.03.050.
[83] Zeng Z, Chen L, Zhu F, Liu X. Dynamic recrystallization behavior of a heat-resistant martensitic stainless steel 403Nb during hot deformation. J Mater Sci Technol 2011;27:913–9. https://doi.org/10.1016/S1005-0302(11)60164-3.
[84] Zhao C, Zhang J, Yang B, Li YF, Huang JF, Lian Y. Hot deformation characteristics and processing map of 1Cr12Ni2Mo2WVNb martensitic stainless steel. Steel Res Int 2020;91:2000020. https://doi.org/10.1002/srin.202000020.
[85] Zhong J, Xiao YH, Guo C. Constitutive modelling for high temperature behaviour of 12CrNiMoWV martensitic stainless steel. Mater Sci Technol 2012;28:719–26. https://doi.org/10.1179/1743284711Y.0000000129.

[86] Zhou X, Ma W, Feng C, Zhang L. Flow stress modeling, processing maps and microstructure evolution of 05Cr17Ni4Cu4Nb Martensitic stainless steel during hot plastic deformation. Mater Res Express 2020;7:46518. https://doi.org/10.1088/2053-1591/ab89d8.
[87] Zou D, Han Y, Yan D, Wang D, Zhang W, Fan G. Hot workability of 00Cr13Ni5Mo2 supermartensitic stainless steel. Mater Des 2011;32:4443–8. https://doi.org/10.1016/j.matdes.2011.03.067.
[88] Wang J, Ma W, Chu Z, Zhang Q. Constitutive model for F45V microalloyed forging steel at high temperature. J Iron Steel Res Int 2014;21:464–8. https://doi.org/10.1016/S1006-706X(14)60072-8.
[89] Lin YC, Chen M-S, Zhong J. Constitutive modeling for elevated temperature flow behavior of 42CrMo steel. Comput Mater Sci 2008;42:470–7. https://doi.org/10.1016/j.commatsci.2007.08.011.
[90] Cho S-H, Yoo Y-C. Hot rolling simulations of austenitic stainless steel. J Mater Sci 2001;36:4267–72. https://doi.org/10.1023/A:1017949812425.
[91] Baragar DL. The high temperature and high strain-rate behaviour of a plain carbon and an HSLA steel. J Mech Work Technol 1987;14:295–307. https://doi.org/10.1016/0378-3804(87)90015-5.
[92] Cingara A, McQueen HJ. New formula for calculating flow curves from high temperature constitutive data for 300 austenitic steels. J Mater Process Technol 1992;36:31–42. https://doi.org/10.1016/0924-0136(92)90236-L.
[93] Johnson GR, Cook WH. A constitutive model and data for metals subjected to large strains, high strain rates and high temperatures. 2018.
[94] Zhang H, Wen W, Cui H. Behaviors of IC10 alloy over a wide range of strain rates and temperatures: experiments and modeling. Mater Sci Eng, A 2009;504:99–103. https://doi.org/10.1016/j.msea.2008.10.056.
[95] Zhang LN, Li PN, Tang SW, Tang WB, Zhang S. Mechanical behaviors analysis and johnson-cook model establishment of 4Cr13 stainless steel. Key Eng Mater 2014;589–590:45–51. https://doi.org/10.4028/www.scientific.net/KEM.589-590.45.
[96] Korkmaz ME, Günay M. Finite element modelling of cutting forces and power consumption in turning of AISI 420 martensitic stainless steel. Arabian J Sci Eng 2018;43:4863–70. https://doi.org/10.1007/s13369-018-3204-4.
[97] Krishna SC, Anoop S, Koundinya NTBN, Karthick NK, Muneshwar P, Pant B. Constitutive modelling of hot deformation behaviour of nitrogen alloyed martensitic stainless steel. Trans. Indian Natl. Acad. Eng. 2020;5:769–77. https://doi.org/10.1007/s41403-020-00182-y.
[98] Estrin Y, Mecking H. A unified phenomenological description of work hardening and creep based on one-parameter models. Acta Metall 1984;32:57–70. https://doi.org/10.1016/0001-6160(84)90202-5.
[99] Wang R, Wang M, Li Z, Lu C. Physics-based constitutive model for the hot deformation of 2Cr11Mo1VNbN martensitic stainless steel. J Mater Eng Perform 2018;27:4932–40. https://doi.org/10.1007/s11665-018-3527-z.
[100] Momeni A, Dehghani K, Ebrahimi GR. Modeling the initiation of dynamic recrystallization using a dynamic recovery model. J Alloys Compd 2011;509:9387–93. https://doi.org/10.1016/j.jallcom.2011.07.014.
[101] Safara N, Engberg G, Ågren J. Modeling microstructure evolution in a martensitic stainless steel subjected to hot working using a physically based model. Metall Mater Trans 2019;50:1480–8. https://doi.org/10.1007/s11661-018-5073-6.
[102] Taylor GI. The mechanism of plastic deformation of crystals. Part I.—Theoretical. Proc R Soc Lond - Ser A Contain Pap a Math Phys Character 1934;145:362–87. https://doi.org/10.1098/rspa.1934.0106.
[103] Prasad YVRK, Gegel HL, Doraivelu SM, Malas JC, Morgan JT, Lark KA, et al. Modeling of dynamic material behavior in hot deformation: forging of Ti-6242. Metall Trans A 1984;15:1883–92. https://doi.org/10.1007/BF02664902.
[104] Prasad YVRK. Processing maps: a status report. J Mater Eng Perform 2003;12:638–45. https://doi.org/10.1361/105994903322692420.
[105] Prasad YVRK, Ravichandran N. Effect of stacking fault energy on the dynamic recrystallization during hot working of FCC metals: a study using processing maps. Bull Mater Sci 1991;14:1241–8. https://doi.org/10.1007/BF02744618.
[106] Ziegler H. In: Grioli G, editor. Thermodynamic aspects of continuum mechanics SBT - proprietà di media e teoremi di confronto in fisica matematica. Berlin, Heidelberg: Springer Berlin Heidelberg; 2011. p. 133–61. ISBN 978-3-642-11018-4.
[107] Tan YB, Yang LH, Tian C, Liu WC, Liu RP, Zhang XY. Processing maps for hot working of 47Zr–45Ti–5Al–3V alloy. Mater Sci Eng, A 2014;597:171–7. https://doi.org/10.1016/j.msea.2013.12.085.
[108] Dadras P, Thomas JF. Characterization and modeling for forging deformation of Ti-6Ai-2Sn-4Zr-2Mo-0.1 Si. Metall Trans A 1981;12:1867–76. https://doi.org/10.1007/BF02643797.
[109] Murty SVSN, Rao BN. On the development of instability criteria during hot working with reference to IN 718. Mater Sci Eng, A 1998;254:76–82. https://doi.org/10.1016/S0921-5093(98)00764-3.
[110] Narayana Murty SVS, Nageswara Rao B, Kashyap BP. Instability criteria for hot deformation of materials. Int Mater Rev 2000;45:15–26. https://doi.org/10.1179/095066000771048782.
[111] Murillo-Marrodán A, Puchi-Cabrera ES, García E, Dubar M, Cortés F, Dubar L. An incremental physically-based model of P91 steel flow behaviour for the numerical analysis of hot-working processes. Met 2018;8.
[112] Ji H, Cai Z, Pei W, Huang X, Lu Y. DRX behavior and microstructure evolution of 33Cr23Ni8Mn3N: experiment and finite element simulation. J Mater Res Technol 2020;9:4340–55. https://doi.org/10.1016/j.jmrt.2020.02.059.
[113] Li C, Tan Y, Zhao F. Dynamic recrystallization behaviour of H13-mod steel. J Iron Steel Res Int 2020;27:1073–86. https://doi.org/10.1007/s42243-020-00462-5.
[114] Sellars CM, Davies GJ, Metallurgical S. Hot working and forming processes : proceedings of an international conference on hot working and forming processes. 1980.
[115] Baron TJ, Khlopkov K, Pretorius T, Balzani D, Brands D, Schröder J. Modeling of microstructure evolution with dynamic recrystallization in finite element simulations of martensitic steel. Steel Res Int 2016;87:37–45. https://doi.org/10.1002/srin.201400576.
[116] Donnay B, Herman JC, Schmitz A, For Science, R.; Development; Commission, E.. Computer assisted modelling of metallurgical aspects of hot deformation and transformation of steels (phase 2). OPOCE; 1999.
[117] Chen F, Ren F, Chen J, Cui Z, Ou H. Microstructural modeling and numerical simulation of multi-physical fields for martensitic stainless steel during hot forging process of turbine blade. Int J Adv Manuf Technol 2016;82:85–98. https://doi.org/10.1007/s00170-015-7368-8.
[118] Chen F, Cui Z, Liu J, Chen W, Chen S. Mesoscale simulation of the high-temperature austenitizing and dynamic recrystallization by coupling a cellular automaton with a topology deformation technique. Mater Sci Eng, A 2010;527:5539–49. https://doi.org/10.1016/j.msea.2010.05.021.

[119] Ma X, Zheng C-W, Zhang X-G, Li D-Z. Microstructural depictions of austenite dynamic recrystallization in a low-carbon steel: a cellular automaton model. Acta Metall Sin (English Lett. 2016;29:1127–35. https://doi.org/10.1007/s40195-016-0502-2.
[120] Chen F, Qi K, Cui Z, Lai X. Modeling the dynamic recrystallization in austenitic stainless steel using cellular automaton method. Comput Mater Sci 2014;83:331–40. https://doi.org/10.1016/j.commatsci.2013.11.029.
[121] Ebrahimi F, Saeidi N, Raeissi M. Microstructural modifications of dual-phase steels: an overview of recent progress and challenges. Steel Res Int 2020;91:2000178. https://doi.org/10.1002/srin.202000178.
[122] Li L, Wang L. Simulation of dynamic recrystallization behavior under hot isothermal compressions for as-extruded 3Cr20Ni10W2 heat-resistant alloy by cellular automaton model. High Temp Mater Process 2018;37:635–47. https://doi.org/10.1515/htmp-2017-0025. doi.
[123] Svyetlichnyy DS. Simulation of microstructure evolution during shape rolling with the use of frontal cellular automata. ISIJ Int 2012;52:559–68. https://doi.org/10.2355/isijinternational.52.559.
[124] Zhang T, Li L, Lu S-H, Gong H, Wu Y-X. Comparisons of different models on dynamic recrystallization of plate during asymmetrical shear rolling. Mater 2018;11.
[125] Takeshita T, Harass J, Yada H. Effects of α_??_γ partial transformation on recrystallization after hot deformation in 17% Cr stainless steel. Trans Iron Steel Inst Japan 1987;27:432–8. https://doi.org/10.2355/isijinternational1966.27.432.
[126] Gao J, Jiang S, Zhang H, Huang Y, Guan D, Xu Y, et al. Facile route to bulk ultrafine-grain steels for high strength and ductility. Nature 2021;590:262–7. https://doi.org/10.1038/s41586-021-03246-3.
[127] Cao P. The strongest size in gradient nanograined metals. Nano Lett 2020;20:1440–6. https://doi.org/10.1021/acs.nanolett.9b05202.
[128] Asaro RJ. Crystal plasticity. J Appl Mech 1983;50:921–34. https://doi.org/10.1115/1.3167205.
[129] Peirce D, Asaro RJ, Needleman A. Material rate dependence and localized deformation in crystalline solids. Acta Metall 1983;31:1951–76. https://doi.org/10.1016/0001-6160(83)90014-7.
[130] Asaro RJ, Rice JR. Strain localization in ductile single crystals. J Mech Phys Solid 1977;25:309–38. https://doi.org/10.1016/0022-5096(77)90001-1.
[131] Iwabuchi Y, Kobayashi I. A study of toughness degradation in CA6NM stainless steel. Mater Sci Forum 2010;654–656:2515–8. https://doi.org/10.4028/www.scientific.net/MSF.654-656.2515.
[132] Roters F, Eisenlohr P, Hantcherli L, Tjahjanto DD, Bieler TR, Raabe D. Overview of constitutive laws, kinematics, homogenization and multiscale methods in crystal plasticity finite-element modeling: theory, experiments, applications. Acta Mater 2010;58:1152–211. https://doi.org/10.1016/j.actamat.2009.10.058.
[133] Maire L, Fausty J, Bernacki M, Bozzolo N, De Micheli P, Moussa C. A new topological approach for the mean field modeling of dynamic recrystallization. Mater Des 2018;146:194–207. https://doi.org/10.1016/j.matdes.2018.03.011.
[134] Ruiz Sarrazola DA, Maire L, Moussa C, Bozzolo N, Pino Muñoz D, Bernacki M. Full field modeling of dynamic recrystallization in a CPFEM context – application to 304L steel. Comput Mater Sci 2020;184:109892. https://doi.org/10.1016/j.commatsci.2020.109892.
[135] Lee M-G, Kim S-J, Han HN. Crystal plasticity finite element modeling of mechanically induced martensitic transformation (MIMT) in metastable austenite. Int J Plast 2010;26:688–710. https://doi.org/10.1016/j.ijplas.2009.10.001.
[136] Wang P, Xiao N, Lu S, Li D, Li Y. Investigation of the mechanical stability of reversed austenite in 13%Cr–4%Ni martensitic stainless steel during the uniaxial tensile test. Mater Sci Eng, A 2013;586:292–300. https://doi.org/10.1016/j.msea.2013.08.028.
[137] Khodabakhshi F, Derazkola HA, Gerlich AP. Monte Carlo simulation of grain refinement during friction stir processing. J Mater Sci 2020;55:13438–56. https://doi.org/10.1007/s10853-020-04963-2.
[138] Roberts W, Ahlblom B. A nucleation criterion for dynamic recrystallization during hot working. Acta Metall 1978;26:801–13. https://doi.org/10.1016/0001-6160(78)90030-5.
[139] Sah JP, Richardson GJ, Sellars CM. Grain-size effects during dynamic recrystallization of nickel. Met Sci 1974;8:325–31. https://doi.org/10.1179/msc.1974.8.1.325.
[140] Sandström R, Lagneborg R. A model for hot working occurring by recrystallization. Acta Metall 1975;23:387–98. https://doi.org/10.1016/0001-6160(75)90132-7.
[141] Sellars CM, Whiteman JA. Recrystallization and grain growth in hot rolling. Met Sci 1979;13:187–94. https://doi.org/10.1179/msc.1979.13.3-4.187.
[142] Price CW. Use of Kolmogorov-Johnson-Mehl-Avrami kinetics in recrystallization of metals and crystallization of metallic glasses. Acta Metall Mater 1990;38:727–38. https://doi.org/10.1016/0956-7151(90)90024-B.
[143] Mecking H, Kocks UF. Kinetics of flow and strain-hardening. Acta Metall 1981;29:1865–75. https://doi.org/10.1016/0001-6160(81)90112-7.
[144] Mohamed G, Bacroix B. Role of stored energy in static recrystallization of cold rolled copper single and multicrystals. Acta Mater 2000;48:3295–302. https://doi.org/10.1016/S1359-6454(00)00155-5.
[145] Kazeminezhad M. On the modeling of the static recrystallization considering the initial grain size effects. Mater Sci Eng, A 2008;486:202–7. https://doi.org/10.1016/j.msea.2007.08.071.
[146] Pietrzyk M. Through-process modelling of microstructure evolution in hot forming of steels. J Mater Process Technol 2002;125–126:53–62. https://doi.org/10.1016/S0924-0136(02)00285-6.
[147] Hou XY, Xu YB, Wu D. Hot deformation behavior of a new-generation 980 MPa grade TRIP steel for automobiles. Adv Mater Res 2011;261–263:775–9. https://doi.org/10.4028/www.scientific.net/AMR.261-263.775.
[148] Laasraoui A, Jonas JJ. Prediction of temperature distribution, flow stress and microstructure during the multipass hot rolling of steel plate and strip. ISIJ Int 1991;31:95–105. https://doi.org/10.2355/isijinternational.31.95.
[149] Humphreys FJ, Hatherly MBT-R, R.A.P., editors. Appendix 2 the measurement of recrystallization. 2nd ed. Oxford: Elsevier; 2004. p. 541–56. ISBN 978-0-08-044164-1.
[150] Srolovitz DJ, Grest GS, Anderson MP. Computer simulation of recrystallization—I. Homogeneous nucleation and growth. Acta Metall 1986;34:1833–45. https://doi.org/10.1016/0001-6160(86)90128-8.
[151] Srolovitz DJ, Anderson MP, Sahni PS, Grest GS. Computer simulation of grain growth—II. Grain size distribution, topology, and local dynamics. Acta Metall 1984;32:793–802. https://doi.org/10.1016/0001-6160(84)90152-4.
[152] Rollett AD, Srolovitz DJ, Anderson MP, Doherty RD. Computer simulation of recrystallization—III. Influence of a dispersion of fine particles. Acta Metall Mater 1992;40:3475–95. https://doi.org/10.1016/0956-7151(92)90062-J.

[153] Anderson MP, Srolovitz DJ, Grest GS, Sahni PS. Computer simulation of grain growth—I. Kinetics. Acta Metall 1984;32:783–91. https://doi.org/10.1016/0001-6160(84)90151-2.
[154] Beck M, Morse M, Corolewski C, Fritchman K, Stifter C, Poole C, et al. Understanding the effect of grain boundary character on dynamic recrystallization in stainless steel 316L. Metall Mater Trans A 2017;48:3831–42. https://doi.org/10.1007/s11661-017-4133-7.
[155] Hore S, Das SK, Banerjee S, Mukherjee S. A multiscale coupled Monte Carlo model to characterize microstructure evolution during hot rolling of Mo-TRIP steel. Acta Mater 2013;61:7251–9. https://doi.org/10.1016/j.actamat.2013.08.030.
[156] Zhang Y, Zhou J, Yin Y, Shen X, Ji X. Multi-GPU implementation of a cellular automaton model for dendritic growth of binary alloy. J Mater Res Technol 2021;14:1862–72. https://doi.org/10.1016/j.jmrt.2021.07.095.
[157] de Castro MH, da Luz JAM, de O. Milhomem F. Cellular automaton-based simulation of bulk stacking and recovery. J Mater Res Technol 2022;16:263–75. https://doi.org/10.1016/j.jmrt.2021.11.127.
[158] Janssens KGF. An introductory review of cellular automata modeling of moving grain boundaries in polycrystalline materials. Math Comput Simulat 2010;80:1361–81. https://doi.org/10.1016/j.matcom.2009.02.011.
[159] Rollett AD, Raabe D. A hybrid model for mesoscopic simulation of recrystallization. Comput Mater Sci 2001;21:69–78. https://doi.org/10.1016/S0927-0256(00)00216-0.
[160] Singh SB, Bhadeshia HKDH. Topology of grain deformation. Mater Sci Technol 1998;14:832–4. https://doi.org/10.1179/mst.1998.14.8.832.
[161] Han C, Jiang P, Geng S, Mi G, Wang C, Li Y. Nucleation mechanisms of equiaxed grains in the fusion zone of aluminum-lithium alloys by laser welding. J Mater Res Technol 2021;14:2219–32. https://doi.org/10.1016/j.jmrt.2021.07.150.
[162] Derby B, Ashby MF. On dynamic recrystallisation. Scripta Metall 1987;21:879–84. https://doi.org/10.1016/0036-9748(87)90341-3.
[163] Peczak P, Luton MJ. The effect of nucleation models on dynamic recrystallization I. Homogeneous stored energy distribution. Philos Mag B 1993;68:115–44. https://doi.org/10.1080/13642819308215285.
[164] Ding R, Guo ZX. Coupled quantitative simulation of microstructural evolution and plastic flow during dynamic recrystallization. Acta Mater 2001;49:3163–75. https://doi.org/10.1016/S1359-6454(01)00233-6.
[165] Ding R, Guo ZX. Microstructural evolution of a Ti–6Al–4V alloy during β-phase processing: experimental and simulative investigations. Mater Sci Eng, A 2004;365:172–9. https://doi.org/10.1016/j.msea.2003.09.024.
[166] Ding R, Guo ZX. Microstructural modelling of dynamic recrystallisation using an extended cellular automaton approach. Comput Mater Sci 2002;23:209–18. https://doi.org/10.1016/S0927-0256(01)00211-7.
[167] Kugler G, Turk R. Modeling the dynamic recrystallization under multi-stage hot deformation. Acta Mater 2004;52:4659–68. https://doi.org/10.1016/j.actamat.2004.06.022.
[168] Cram DG, Zurob HS, Brechet YJM, Hutchinson CR. Modelling discontinuous dynamic recrystallization using a physically based model for nucleation. Acta Mater 2009;57:5218–28. https://doi.org/10.1016/j.actamat.2009.07.024.
[169] Zou D, Liu X, Han Y, Zhang W, Li J, Wu K. Influence of heat treatment temperature on microstructure and property of 00Cr13Ni5Mo2 supermartensitic stainless steel. J Iron Steel Res Int 2014;21:364–8. https://doi.org/10.1016/S1006-706X(14)60056-X.
[170] Jin Z, Cui Z. Investigation on strain dependence of dynamic recrystallization behavior using an inverse analysis method. Mater Sci Eng, A 2010;527:3111–9. https://doi.org/10.1016/j.msea.2010.01.062.
[171] Wang W, Man T, Zhang M, Wang Y, Dong H. δ-ferrite dynamic recrystallization behavior during thermal deformation in Fe–32Mn–11Al-0.9C low density steel. J Mater Res Technol 2022;18:1345–57. https://doi.org/10.1016/j.jmrt.2022.02.129.
[172] Du Z, Liu X, Gui J, Ke Y, Zhang L. Influence of MnS inclusions on dynamic recrystallization and annealing twins formation during thermal deformation. J Mater Res Technol 2022;16:1371–87. https://doi.org/10.1016/j.jmrt.2021.12.088.
[173] Razali MK, Joun MS. A new approach of predicting dynamic recrystallization using directly a flow stress model and its application to medium Mn steel. J Mater Res Technol 2021;11:1881–94. https://doi.org/10.1016/j.jmrt.2021.02.026.
[174] Zhou X, Zhang H, Wang G, Bai X, Fu Y, Zhao J. Simulation of microstructure evolution during hybrid deposition and micro-rolling process. J Mater Sci 2016;51:6735–49. https://doi.org/10.1007/s10853-016-9961-0.
[175] Wang L, Fang G, Qian L. Modeling of dynamic recrystallization of magnesium alloy using cellular automata considering initial topology of grains. Mater Sci Eng, A 2018;711:268–83. https://doi.org/10.1016/j.msea.2017.11.024.
[176] Zheng C, Xiao N, Li D, Li Y. Mesoscopic modeling of austenite static recrystallization in a low carbon steel using a coupled simulation method. Comput Mater Sci 2009;45:568–75. https://doi.org/10.1016/j.commatsci.2008.11.021.
[177] Yazdipour N, Davies CHJ, Hodgson PD. Microstructural modeling of dynamic recrystallization using irregular cellular automata. Comput Mater Sci 2008;44:566–76. https://doi.org/10.1016/j.commatsci.2008.04.027.
[178] Chen F, Cui Z, Liu J, Zhang X, Chen W. Modeling and simulation on dynamic recrystallization of 30Cr2Ni4MoV rotor steel using the cellular automaton method. Model Simulat Mater Sci Eng 2009;17:75015. https://doi.org/10.1088/0965-0393/17/7/075015.
[179] Riedel H, Svoboda J. A model for strain hardening, recovery, recrystallization and grain growth with applications to forming processes of nickel base alloys. Mater Sci Eng, A 2016;665:175–83. https://doi.org/10.1016/j.msea.2016.04.015.
[180] Chen M-S, Yuan W-Q, Lin YC, Li H-B, Zou Z-H. Modeling and simulation of dynamic recrystallization behavior for 42CrMo steel by an extended cellular automaton method. Vacuum 2017;146:142–51. https://doi.org/10.1016/j.vacuum.2017.09.041.
[181] Qian M, Guo ZX. Cellular automata simulation of microstructural evolution during dynamic recrystallization of an HY-100 steel. Mater Sci Eng, A 2004;365:180–5. https://doi.org/10.1016/j.msea.2003.09.025.
[182] Wang Y, Xing X, Zhang Y, Jiang S. Investigation of the dynamic recrystallization of FeMnSiCrNi shape memory alloy under hot compression based on cellular automaton. Met 2019;9.
[183] Chen F, Zhu H, Zhang H, Cui Z. Mesoscale modeling of dynamic recrystallization: multilevel cellular automaton simulation framework. Metall Mater Trans A 2020;51:1286–303. https://doi.org/10.1007/s11661-019-05620-3.
[184] Wu C, Jia B, Han S. Coupling a cellular automaton model with a finite element model for simulating deformation and recrystallization of a low-carbon micro-alloyed steel during hot compression. J Mater Eng Perform 2019;28:938–55. https://doi.org/10.1007/s11665-018-3834-4.
[185] Zhi Y, Liu X, Yu H. Cellular automaton simulation of hot deformation of TRIP steel. Comput Mater Sci

2014;81:104–12. https://doi.org/10.1016/j.commatsci.2013.05.028.
[186] Chen X, Zhang J, Du Y, Wang G, Huang T. Dynamic recrystallization simulation for X12 alloy steel by CA method based on modified L-J dislocation density model. Met 2019;9.
[187] Guo Z, Sha W. Modelling the correlation between processing parameters and properties of maraging steels using artificial neural network. Comput Mater Sci 2004;29:12–28. https://doi.org/10.1016/S0927-0256(03)00092-2.
[188] Krizhevsky A, Sutskever I, Hinton GE. ImageNet classification with deep convolutional neural networks. In: Pereira F, Burges CJC, Bottou L, Weinberger KQ, editors. Proceedings of the advances in neural information processing systems, vol. 25. New York, NY, USA: Association for Computing Machinery; 2017. p. 84–90.
[189] Cireşan D, Schmidhuber J. Multi-column deep neural networks for offline handwritten Chinese character classification. 2013.
[190] Coit DW, Smith AE. Using designed experiments to produce robust neural network models of manufacturing processes. 1995.
[191] Benardos PG, Vosniakos GC. Prediction of surface roughness in CNC face milling using neural networks and Taguchi's design of experiments. Robot Comput Integrated Manuf 2002;18:343–54. https://doi.org/10.1016/S0736-5845(02)00005-4.
[192] Benardos PG, Mosialos S, Vosniakos G-C. Prediction of workpiece elastic deflections under cutting forces in turning. Robot Comput Integrated Manuf 2006;22:505–14. https://doi.org/10.1016/j.rcim.2005.12.009.
[193] Arriandiaga A, Portillo E, Sánchez JA, Cabanes I, Pombo I. A new approach for dynamic modelling of energy consumption in the grinding process using recurrent neural networks. Neural Comput Appl 2016;27:1577–92. https://doi.org/10.1007/s00521-015-1957-1.
[194] Sanchez JA, Conde A, Arriandiaga A, Wang J, Plaza S. Unexpected event prediction in wire electrical Discharge machining using deep learning techniques. Mater 2018;11.
[195] Mandal S, Sivaprasad PV, Venugopal S, Murthy KPN. Constitutive flow behaviour of austenitic stainless steels under hot deformation: artificial neural network modelling to understand, evaluate and predict. Model Simulat Mater Sci Eng 2006;14:1053–70. https://doi.org/10.1088/0965-0393/14/6/012.
[196] Mandal S, Sivaprasad PV, Barat P, Raj B. An overview of neural network based modeling in alloy design and thermomechanical processing of austenitic stainless steels. Mater Manuf Process 2009;24:219–24. https://doi.org/10.1080/10426910802612361.
[197] Rumelhart DE, Hinton GE, Williams RJ. Learning representations by back-propagating errors. Nature 1986;323:533–6. https://doi.org/10.1038/323533a0.
[198] Srinivasulu S, Jain A. A comparative analysis of training methods for artificial neural network rainfall–runoff models. Appl Soft Comput 2006;6:295–306. https://doi.org/10.1016/j.asoc.2005.02.002.
[199] Mandal S, Sivaprasad PV, Venugopal S, Murthy KPN. Artificial neural network modeling to evaluate and predict the deformation behavior of stainless steel type AISI 304L during hot torsion. Appl Soft Comput 2009;9:237–44. https://doi.org/10.1016/j.asoc.2008.03.016.
[200] Mandal S, Sivaprasad PV, Venugopal S, Murthy KPN, Raj B. Artificial neural network modeling of composition–process–property correlations in austenitic stainless steels. Mater Sci Eng, A 2008;485:571–80. https://doi.org/10.1016/j.msea.2007.08.019.
[201] Gupta AK, Singh SK, Reddy S, Hariharan G. Prediction of flow stress in dynamic strain aging regime of austenitic stainless steel 316 using artificial neural network. Mater Des 2012;35:589–95. https://doi.org/10.1016/j.matdes.2011.09.060.
[202] Singh K, Rajput SK, Soota T, Verma V, Singh D. Prediction of hot deformation behavior of high phosphorus steel using artificial neural network. IOP Conf Ser Mater Sci Eng 2018;330:12038. https://doi.org/10.1088/1757-899x/330/1/012038.
[203] Han Y, Qiao GJ, Yan DN, Zou DN. Artificial neural network to predict the hot deformation behavior of super 13Cr martensitic stainless steel. Mater Sci Forum 2011;695:361–4. https://doi.org/10.4028/www.scientific.net/MSF.695.361.
[204] Shokry A, Gowid S, Kharmanda G, Mahdi E. Constitutive models for the prediction of the hot deformation behavior of the 10%Cr steel alloy. Mater 2019;12.
[205] Levenberg KA. Method for the solution of certain non-linear problems in least squares. Q Appl Math 1944;2:164–8.
[206] Opěla P, Schindler I, Kawulok P, Kawulok R, Rusz S, Navrátil H, et al. Correlation among the power dissipation efficiency, flow stress course, and activation energy evolution in Cr-Mo low-alloyed steel. Mater 2020;13.
[207] Kumar S, Karmakar A, Nath SK. Construction of hot deformation processing maps for 9Cr-1Mo steel through conventional and ANN approach. Mater Today Commun 2021;26:101903. https://doi.org/10.1016/j.mtcomm.2020.101903.